

DISSOLVED MASSIVE METAL-RICH GLOBULAR CLUSTERS CAN CAUSE THE RANGE OF UV UPTURN STRENGTHS FOUND AMONG EARLY-TYPE GALAXIES

PAUL GOUDFROOIJ

Space Telescope Science Institute, 3700 San Martin Drive, Baltimore, MD 21218, USA; goudfroo@stsci.edu

Received 2018 February 8; revised 2018 February 28; accepted 2018 March 4; published 2018 April 9

ABSTRACT

I discuss a scenario in which the ultraviolet (UV) upturn of giant early-type galaxies (ETGs) is primarily due to helium-rich stellar populations that formed in massive metal-rich globular clusters (GCs) which subsequently dissolved in the strong tidal field in the central regions of the massive host galaxy. These massive GCs are assumed to show UV upturns similar to those observed recently in M87, the central giant elliptical galaxy in the Virgo cluster of galaxies. Data taken from the literature reveals a strong correlation between the strength of the UV upturn and the specific frequency of metal-rich GCs in ETGs. Adopting a Schechter function parametrization of GC mass functions, simulations of long-term dynamical evolution of GC systems show that the observed correlation between UV upturn strength and GC specific frequency can be explained by variations in the characteristic truncation mass M_c such that M_c increases with ETG luminosity in a way that is consistent with observed GC luminosity functions in ETGs. These findings suggest that the nature of the UV upturn in ETGs and the variation of its strength among ETGs are causally related to that of helium-rich populations in massive GCs, rather than intrinsic properties of field stars in massive galactic spheroids. With this in mind, I predict that future studies will find that $[N/Fe]$ decreases with increasing galactocentric radius in massive ETGs, and that such gradients have the largest amplitudes in ETGs with the strongest UV upturns.

Keywords: galaxies: stellar content — galaxies: bulges — galaxies: star clusters: general — globular clusters: general

1. INTRODUCTION

Starting in the 1970's, various ultraviolet (UV) space observatory missions have firmly established that luminous early-type galaxies (hereafter ETGs) and bulges of spiral galaxies feature far-UV (FUV) emission whose strength rises shortwards of $\sim 2000 \text{ \AA}$ (e.g., Code & Welch 1979; Bertola 1980; Burstein et al. 1988; O'Connell et al. 1992; Dorman et al. 1995; Brown et al. 1997). This phenomenon is widely known as the "UV upturn," which was originally unexpected because ETGs were generally believed to be old "red and dead" stellar populations.

Studies of the UV-to-optical spectral energy distribution of ETGs showed that the UV upturn is well-fit by a narrow range of effective temperatures between $\sim 20,000$ and $25,000 \text{ K}$ (e.g., Brown et al. 1997). It is commonly believed that the UV upturn in ETGs is mainly produced by extreme horizontal branch (EHB) stars, also known as hot subdwarfs, and their progeny (see, e.g., the reviews by O'Connell 1999 and Yi 2008). These are helium-core-burning stars with extremely thin hydrogen envelopes. Various scenarios for their formation have been proposed: strong mass loss on the red giant branch (RGB; this likely mainly occurs at high metallicity, see Greggio & Renzini 1990), high helium abundance (e.g., Dorman et al. 1995; Yi et al. 1997), and/or mass transfer of RGB envelopes in binary systems (Han et al. 2007).

Important constraints to the nature of the UV upturn in nearby ETGs were introduced by Burstein et al. (1988) who showed that the $m(1550) - V$ color (hereafter $FUV - V$) anticorrelates strongly with both velocity dispersion (σ) and the Lick Mg_2 absorption-line index. Since the latter was thought to be mainly a metallicity indicator and because σ also correlates strongly with Mg_2 , Burstein et al. argued that stellar metallicity is the fundamental parameter underlying these relations.

Another key feature of the UV upturn in ETGs is that its

spatial distribution is more centrally concentrated than the optical light (Ohl et al. 1998; Carter et al. 2011). As such, matching of measurement apertures between the FUV and other wavelengths is important in the interpretation of correlation studies. This point proved to be relevant in understanding apparent inconsistencies between different studies of the $FUV - V$ versus Mg_2 relation using the *Galaxy Evolution Explorer* (GALEX; Martin et al. 2005): Rich et al. (2005) used a sample of ETGs covering a significant range of distances ($z < 0.2$) along with fixed measurement apertures and did *not* recover the Burstein et al. (1988) relation. However, several other studies used samples of ETGs for which UV and optical measurement apertures were matched on a galaxy-by-galaxy basis (Bureau et al. 2011; Jeong et al. 2012) or samples of cluster galaxies to eliminate the distance effect (Boselli et al. 2005; Smith et al. 2012a). The latter studies all do recover the Burstein et al. (1988) relation (some using the Mgb index rather than Mg_2). Other relations between UV upturn and ETG parameters that were established by these studies were anticorrelations of $FUV - V$ with σ , age, total metallicity $[Z/H]$ and α -element abundance enhancement $[\alpha/Fe]$. These anticorrelations are not expected in the scenario where hot subdwarfs are produced by strong mass transfer of RGB envelopes in binaries, in which the dependence of $FUV - V$ on age and metallicity is insignificant (Han et al. 2007). Consequently, many recent studies of the UV upturn have concentrated on the single-star mechanisms (but see Section 5.1.1).

A pivotal discovery in the context of the nature of the UV upturn was that of massive FUV-bright globular clusters (GCs) in M87, the central galaxy of the Virgo cluster¹ (Sohn et al. 2006; see also Peacock et al. 2017). Many of those GCs in M87 were found to feature $FUV - V$ colors similar to, or even

¹ To date, M87 is the only ETG with a UV upturn for which FUV photometry of GCs has been published.

bluer than, ETGs with the strongest UV upturns. Interestingly, several massive *metal-rich* GCs in M87 have both $FUV-V$ and $NUV-V$ colors consistent with those of massive ETGs². Among metal-rich GCs in our Galaxy, this behavior is only seen in NGC 6388 and NGC 6441, two massive GCs with very hot EHBs (see Rich et al. 1997), which are thought to be due to a high He abundance in a significant fraction of their constituent stars (Caloi & D’Antona 2007; Tailo et al. 2017).

In fact, a myriad of recent studies of multiple stellar populations in GCs in the Local Group revealed that light-element abundance variations within massive GCs are the norm rather than the exception (see, e.g., the review by Gratton et al. 2012). The strongest abundance patterns emerging from spectroscopic studies of GCs are that $[Na/Fe]$ correlates with $[N/Fe]$ and generally anticorrelates with $[O/Fe]$ and $[C/Fe]$ (e.g., Snedden et al. 1992; Roediger et al. 2014). These patterns are thought to be the result of proton-capture reactions at $T \gtrsim 2 \times 10^7$ K such as the CNO and NeNa cycles (e.g., Gratton et al. 2012). The material responsible for these abundance variations is generally thought to originate in winds of stars massive enough to host such high temperatures in their interiors (“polluters”). Subsequent episodes of star formation in GCs with masses and escape velocities high enough to retain these winds may have caused the abundance variations seen today within such GCs (see, e.g., D’Ercole et al. 2008; Goudfrooij et al. 2011; Conroy 2012; Renzini et al. 2015).

Recent studies have shown that GC mass is indeed an important parameter in the context of light-element abundance variations in GCs. Its relevance was first suggested by the results of Carretta et al. (2010), who showed that the extent of the Na–O anticorrelation within GCs scales with GC mass. More recently, Milone et al. (2017) studied high-precision *Hubble Space Telescope* (*HST*) photometry of RGB stars in 57 Galactic GCs using a selection of filters that emphasizes abundance spreads in N and O. They found a strong correlation between the fraction of stars enhanced in $[N/Fe]$ and the GC mass. Furthermore, studies using integrated-light spectroscopy of GCs in M31 and our Galaxy show a similarly strong correlation between overall $[N/Fe]$ and GC mass (Schiavon et al. 2013; T. H. Puzia & P. Goudfrooij 2018, in preparation).

Importantly with regard to the UV upturn, the proton-capture processes at high temperatures that produce enhancements in $[N/Fe]$ and $[Na/Fe]$ also produce He enhancement, one of the main contenders for producing the hot EHB stars in GCs, including those in M87 (see Kaviraj et al. 2007). While direct measurements of the He abundance (hereafter Y) are generally difficult to obtain for stellar populations, it is well known that increases in Y cause hotter and bluer main sequences in color-magnitude diagrams (e.g., Dotter et al. 2007; Piotto et al. 2007; Cassisi et al. 2017). This effect was used by Milone (2015) to show that the spread in Y found within Galactic GCs is strongly correlated with GC mass, similar to the case of $[N/Fe]$ spread mentioned above. This correlation is consistent with recent photometric studies of HB stars in GCs using *HST*, which clearly indicate a need for significant He enhancement to fit the multi-color photometry of the HBs in the most massive GCs and to explain the finding that the hottest types of HB stars (“blue-hook stars”) exist only in the most massive GCs (Brown et al. 2010, 2016).

² In contrast, the metal-poor GCs in M87 generally feature bluer UV–optical colors than those of ETGs with UV upturns, especially in $NUV-V$, which is likely due to metallicity-dependent line blanketing in the NUV (e.g., Dorman et al. 1995).

In this paper, we investigate the idea that there is a physical connection between the UV upturn in ETGs and the He-enhanced populations in massive GCs. This connection was suggested earlier: Chung et al. (2011) constructed simple stellar population (SSP) models including effects of He enhancement and showed that the UV upturns of ETGs are well fit by their models, while Bekki (2012) studied this connection using numerical simulations. Here, we explore the possibility that the range of UV upturn strengths found among ETGs is caused by He-rich stars formed in massive GCs that subsequently disrupted in the strong tidal field of the inner regions of their host galaxies.

2. GC SYSTEMS IN EARLY-TYPE GALAXIES

While GCs typically constitute a very small fraction of the stellar mass in “normal” galaxies, their properties contain important clues to the assembly histories of their host galaxies. Infrared studies of star formation within molecular clouds have shown that stars typically form in a clustered fashion (bound clusters or unbound associations; Lada & Lada 2003; Portegies Zwart et al. 2010). Most star clusters with initial masses $M_0 \lesssim 10^4 M_\odot$ are thought to evaporate into the field population of galaxies within a few Gyr, but the currently surviving massive GCs represent important probes of the chemical evolution occurring during the main epochs of star formation within a galaxy’s assembly history.

One of the most studied observational parameters in the context of the GC–galaxy connection is the *specific frequency* of GCs (hereafter S_N). This parameter was introduced by Harris & van den Bergh (1981), who defined it as the number of GCs per unit galaxy luminosity in units of $M_V = -15$. S_N essentially measures the number of GCs that survived dynamical evolution over the galaxy’s lifespan relative to the total luminosity of stars that evaporated *out of* star clusters or associations during that period. As such, its value is determined by the shape of the initial cluster mass function (ICMF) and the time-dependent effects of dynamical evolution of GCs.³

Several studies have established that S_N varies greatly among galaxies. The general trend among massive galaxies is that S_N increases significantly with increasing galaxy luminosity: S_N for the most luminous ETGs (with $M_V \sim -23$) is a factor of ~ 5 higher on average than that for ETGs with $M_V \sim -20$ (Peng et al. 2008). Conversely, the trend is opposite among galaxies fainter than $M_V \sim -20$, for which S_N increases with *decreasing* galaxy luminosity, with several faint dwarf galaxies with $-16 \lesssim M_V \lesssim -12$ showing S_N values larger than those of the most luminous ETGs (e.g., Forbes 2005; Miller & Lotz 2007; Peng et al. 2008; Georgiev et al. 2010; Harris et al. 2013).

Deep imaging studies with the *HST* and large ground-based telescopes have shown that “normal” luminous ETGs typically contain rich GC systems featuring wide, bimodal optical color distributions (e.g., Brodie & Strader 2006; Peng et al. 2006). Spectroscopy showed that such GCs are nearly universally old ($\gtrsim 10$ Gyr), independent of their color (e.g., Puzia et al. 2005; Brodie et al. 2012), implying that their colors mainly indicate differences in metallicity. The “red” GCs feature colors and spatial distributions that generally follow those of the underlying spheroidal light (i.e., the “bulge”), while the “blue” GC subsystems typically show much more extended (“halo-like”) spatial distributions, consistent with those of metal-poor GCs in our Galaxy and M31 (e.g., Geisler et al. 1996; Rhode & Zepf

³ This is discussed further in Sections 4.1 and 5.1.

2004; Brodie & Strader 2006; Harris et al. 2010; Puzia et al. 2014). The overall number ratio $N(\text{red})/N(\text{blue})$ changes with ETG mass or luminosity. Low-mass ETGs with $M_V \gtrsim -18$ host virtually only blue GCs. For more massive ETGs, the fraction of red GCs increases with galaxy luminosity up to $M_V \approx -22$, beyond which it decreases again due to large numbers of blue GCs, mainly located in the outer regions of the most massive ETGs (Peng et al. 2008).

The general picture that has emerged from these studies is that the blue GCs are likely to represent remnants of the earliest stages of hierarchical merging of gas-rich, metal-poor protogalactic dwarfs, which caused high GC formation rates in regions with high star formation rate surface density (e.g., Burgarella et al. 2001; Moore et al. 2006; Peng et al. 2008), while the red GCs were formed during mergers of more massive gas-rich galaxies at high redshift (e.g., Peng et al. 2008; Kruijssen 2015), perhaps situated within more massive halos that were able to retain the chemically enriched gas outflows from earlier star formation episodes. The large numbers of blue GCs found in the outskirts of the most massive ETGs likely reflect relatively large numbers of accreted dwarf galaxies, while the increase in S_N of red GCs with increasing ETG luminosity is thought to indicate an increasing mass fraction of higher-mass protogalaxies that underwent starbursts at high SFR surface density (Ashman & Zepf 1992; Peng et al. 2008; Kruijssen 2015).

3. RELATIONS BETWEEN UV UPTURN STRENGTH AND POPULATION AND GC SYSTEM PROPERTIES

To explore the relevance of the specific frequency of GCs in the production of the UV upturn in ETGs, we select two samples of nearby ETGs based on their source of UV data (IUE vs. GALEX) and the availability of dynamical and stellar population properties as well as GC specific frequency data for both metal-poor and metal-rich GC subpopulations in the literature.

The first sample is a subset of that studied by Dorman et al. (1995), using the aperture-matched IUE, V -band, and Mg_2 data from Burstein et al. (1988). We remove galaxies with strong dust extinction in their inner regions, since this renders a significant uncertainty to their intrinsic $FUV - V$ colors. This eliminates the galaxies NGC 1052, NGC 2768, NGC 4111, NGC 4125, NGC 4278, NGC 4374, and NGC 5846 (Hansen et al. 1985; Goudfrooij et al. 1994b; van Dokkum & Franx 1995; Goudfrooij & Trinchieri 1998; Martel et al. 2004; Lauer et al. 2005; Masegosa et al. 2011). The resulting sample is henceforth referred to as the ‘‘IUE sample.’’ Stellar population parameters for eight galaxies in the IUE sample are taken from Thomas et al. (2005), using spectroscopic measurements of indices $H\beta$, Mgb , $\text{Fe}5270$, and $\text{Fe}5335$ in the Lick system within an aperture of $R_{\text{eff}}/10$, where R_{eff} is the effective radius of the galaxy. The ages, metallicities ($[Z/H]$) and $[\alpha/\text{Fe}]$ ratios are determined using the SSP models of Thomas et al. (2003). For the nine other galaxies in the IUE sample, we use Lick-system line index measurements from other studies (see Table 1) and use the Thomas et al. (2003) SSP models to place their SSP-equivalent ages, $[Z/H]$, and $[\alpha/\text{Fe}]$ measurements in the same system as that of Thomas et al. (2005), using linear interpolation between the model grid points. In this context we use the diagram of $\langle \text{Fe} \rangle$ ($= 0.5 \times (\text{Fe}5270 + \text{Fe}5335)$) versus Mgb to provide a first estimate of the $[\alpha/\text{Fe}]$ ratio, and the $[\text{MgFe}]'$ versus $H\beta$

diagram to estimate the ages and $[Z/H]$ values.⁴ The three population parameters are then modified using a small grid around the first estimates, and the best error-weighted fit to $H\beta$, Mgb , and $\langle \text{Fe} \rangle$ is selected.

The second sample of galaxies is taken from the SAURON project (e.g., de Zeeuw et al. 2002), for which GALEX images and optical spectroscopy were analyzed by Bureau et al. (2011) and Jeong et al. (2012), using measurements in an aperture of $R_e/2$ for each galaxy.

For both galaxy samples, specific frequencies S_N of metal-rich (red) GCs are taken from recent papers in the literature that used high-quality GC colors from data taken with the Advanced Camera for Surveys (ACS) aboard *HST*. References are given in Tables 1 and 2 for the IUE and SAURON samples, respectively. For the Fornax ellipticals NGC 1399 and NGC 1404 in the IUE sample, we determine metal-rich GC fractions from the GC photometry tables of the ACS Fornax Cluster Survey (see Jordán et al. 2015). To stay consistent with the results for Virgo galaxies by the ACS Virgo Cluster Survey, we adopt the procedures and GC selection criteria of Peng et al. (2006) in this context. Briefly, to establish red GC fractions (designated f_{red} in Tables 1 and 2), we apply the Kaye’s Mixture Model (KMM, McLachlan & Basford 1988; Ashman et al. 1994) to fit two Gaussians to the GC color distribution using the homoscedastic case, where σ is the same for both Gaussians. Specific frequencies of red GCs were determined following Peng et al. (2008), normalizing the derived number of such GCs in the galaxy by the galaxy luminosity in the SDSS (Sloan Digital Sky Survey) z passband (similar to the F850LP passband of *HST*/ACS):

$$S_{N, z, \text{red}} = N_{\text{GC, red}} \times 10^{0.4(M_z + 15)} \quad (1)$$

For galaxies in the ACS Virgo Cluster Survey, we adopt the total z -band magnitudes in the AB system from Peng et al. (2008). For other galaxies with S_N data that were derived from total V -band luminosities in the literature, integrated $V - z_{\text{AB}}$ colors are determined in two different ways. For NGC 4889, we simply use the observed integrated $V - z$ color from Eisenhardt et al. (2007), assuming $z_{\text{AB}} = z_{\text{Vega}} + 0.518$. For the other galaxies, z -band photometry is not available and we use high-quality integrated colors in other passbands along with the SSP models of Bruzual & Charlot (2003, hereafter BC03) to estimate $V - z$ as follows. We use NED to obtain the integrated colors $(V - R)_J$ from Persson et al. (1979) for the southern galaxies, and $(g - z)_{\text{SDSS}}$ for NGC 5982. We then determine $(V - R)_J$, $V - z_{\text{AB}}$, and $(g - z)_{\text{SDSS}}$ from a large set of spectral energy distributions from the BC03 SSP models⁵ using the SYNPHOT package within IRAF/STSDAS. Finally, we derive second-order polynomial relations between those colors to derive $V - z_{\text{AB}}$ from $(V - R)_J$ or $(g - z)_{\text{SDSS}}$. The RMS errors of these relations are 0.008 mag between $V - z_{\text{AB}}$ and $(V - R)_J$ and 0.005 mag between $V - z_{\text{AB}}$ and $(g - z)_{\text{SDSS}}$.

Figure 1 shows $FUV - V$ versus the various stellar population parameters, the central velocity dispersion from HyperLeda, and $S_{N, z, \text{red}}$ for the IUE sample. Note that the $m(1550) - V$ magnitudes from Dorman et al. (1995) were transformed to $FUV - V$ in the AB magnitude system using $(FUV - V)_{\text{AB}} = m(1550) - V + 2.75$. The Spearman rank correlation coefficient R_s is mentioned for each relation in the various panels. R_s is measured and shown twice for each relation: once for all

⁴ The $[\text{MgFe}]'$ index was chosen because of its independence of variations in $[\alpha/\text{Fe}]$ ratio and IMF slope (Thomas et al. 2003; Vazdekis et al. 2010).

⁵ This grid of models constituted ages ≥ 5 Gyr and $0.2 \leq Z/Z_\odot \leq 2.5$.

Table 1
Properties of galaxies in IUE sample.

NGC (1)	$(FUV-V)_0$ (2)	Mg ₂ (3)	[Z/H] (4)	[α /Fe] (5)	Age (6)	Ref. (7)	σ (8)	V_{\max} (9)	S_N (10)	$S_{N,z}$ (11)	f_{red} (12)	Ref. (13)
221	4.50 ± 0.17	0.198 ± 0.002	0.152 ± 0.030	-0.025 ± 0.013	2.4 ± 0.2	1	65 ± 2	43 ± 12	—	—	—	—
224	3.46 ± 0.17	0.324 ± 0.002	0.441 ± 0.048	0.219 ± 0.017	7.0 ± 0.8	1	154 ± 4	74 ± 40	—	—	—	—
584	3.93 ± 0.17	0.298 ± 0.004	0.478 ± 0.046	0.223 ± 0.014	2.8 ± 0.3	1	199 ± 4	72 ± 5	—	—	—	—
1399	2.04 ± 0.17	0.357 ± 0.008	0.56 ± 0.12	0.35 ± 0.04	10.0 ± 1.4	2	332 ± 5	37 ± 22	11.5 ± 1.0	4.00 ± 0.35	0.63	1
1404	3.26 ± 0.17	0.344 ± 0.007	0.43 ± 0.09	0.18 ± 0.03	8.9 ± 1.3	2	227 ± 4	96 ± 19	2.0 ± 0.5	0.77 ± 0.20	0.56	1
1407	2.40 ± 0.17	0.341 ± 0.010	0.29 ± 0.13	0.38 ± 0.08	17.0 ± 3.4	3	266 ± 5	35 ± 26	4.0 ± 1.3	1.79 ± 0.58	0.62	2
2784	3.65 ± 0.25	0.334 ± 0.007	0.67 ± 0.07	0.23 ± 0.07	4.5 ± 0.8	4	222 ± 6	173 ± 19	—	—	—	—
3115	3.40 ± 0.17	0.309 ± 0.006	0.20 ± 0.06	0.08 ± 0.05	17.0 ± 4.7	4	259 ± 3	106 ± 5	2.3 ± 0.5	0.98 ± 0.21	0.35	3
3379	3.82 ± 0.17	0.329 ± 0.006	0.299 ± 0.036	0.259 ± 0.012	10.0 ± 1.1	1	203 ± 2	52 ± 11	—	—	—	—
4472	3.39 ± 0.17	0.331 ± 0.005	0.342 ± 0.046	0.258 ± 0.021	9.6 ± 1.4	1	282 ± 3	50 ± 20	5.40 ± 0.57	2.20 ± 0.23	0.29	4
4494	3.77 ± 0.17	0.293 ± 0.009	0.12 ± 0.03	0.14 ± 0.02	14.0 ± 2.9	4	148 ± 3	69 ± 14	—	—	—	—
4552	2.32 ± 0.17	0.346 ± 0.006	0.356 ± 0.034	0.277 ± 0.011	12.4 ± 1.5	1	250 ± 3	6 ± 10	2.82 ± 0.57	1.15 ± 0.23	0.53	4
4621	3.14 ± 0.17	0.355 ± 0.009	0.65 ± 0.09	0.30 ± 0.08	5.6 ± 1.2	4	228 ± 4	109 ± 22	2.70 ± 1.19	1.07 ± 0.47	0.49	4
4649	2.20 ± 0.17	0.360 ± 0.006	0.362 ± 0.029	0.296 ± 0.012	14.1 ± 1.5	1	331 ± 5	55 ± 22	5.16 ± 1.20	2.03 ± 0.47	0.57	4
4697	3.41 ± 0.17	0.320 ± 0.006	0.148 ± 0.043	0.155 ± 0.018	8.3 ± 1.4	1	165 ± 2	105 ± 29	—	—	—	—
4762	3.68 ± 0.17	0.280 ± 0.006	0.23 ± 0.05	0.12 ± 0.05	8.8 ± 2.5	4	141 ± 4	110 ± 19	—	—	—	—
4889	2.71 ± 0.17	0.356 ± 0.008	0.29 ± 0.03	0.28 ± 0.01	15.5 ± 2.9	5	393 ± 5	7 ± 17	5.5 ± 0.1	1.97 ± 0.10	0.60	5

Note. — Column (1): NGC number of galaxy. Column (2): $(FUV-V)_0$ in the STAG system from [Dorman et al. \(1995\)](#). Column (3): Mg₂ index in mag from [Burstein et al. \(1988\)](#). Column (4): [Z/H] in dex. Column (5): [α /Fe] in dex. Column (6): age in Gyr. Column (7): reference of Lick index data used for stellar population parameters (1 = [Thomas et al. 2005](#), 2 = [Kuntschner 2000](#), 3 = [Spolaor et al. 2006](#), 4 = [Trager et al. 1998](#), 5 = [Sánchez-Blázquez et al. 2006](#)). For references other than #1, stellar population parameters were derived as described in the text. Column (8): central velocity dispersion in km s⁻¹ from LEDA. Column (9): maximum rotational velocity in km s⁻¹ from LEDA. Column (10): specific frequency of GCs. Column (11): specific frequency per unit z-band luminosity (see Equation 1). Column (12): fraction of red GCs. Column (13): reference of GC data (1 = this paper, 2 = [Forbes et al. 2006](#), 3 = [Jennings et al. 2014](#), 4 = [Peng et al. 2006](#), 5 = [Harris et al. 2017](#)).

Table 2
Relevant properties of galaxies in SAURON sample with S_N data.

NGC (1)	$(FUV-V)_{\text{AB},0}$ (2)	Age (3)	σ (4)	V_{\max} (5)	S_N (6)	$S_{N,z}$ (7)	f_{red} (8)	Ref. (9)
474	6.76 ± 0.19	8.89 ± 1.54	154 ± 3	30 ± 6	2.10 ± 0.50	0.99 ± 0.24	0.13	1
4387	6.98 ± 0.14	10.34 ± 1.79	100 ± 3	58 ± 6	1.52 ± 0.21	0.65 ± 0.09	0.23	2
4473	6.90 ± 0.06	11.76 ± 2.03	179 ± 3	57 ± 6	1.98 ± 0.51	0.88 ± 0.23	0.43	2
4486	5.36 ± 0.07	17.70 ± 2.04	323 ± 4	20 ± 21	12.59 ± 0.77	4.19 ± 0.25	0.27	2
4570	6.67 ± 0.05	12.82 ± 2.22	187 ± 5	—	1.09 ± 0.18	0.53 ± 0.09	0.36	2
4621	6.32 ± 0.06	13.67 ± 2.36	228 ± 4	109 ± 22	2.70 ± 1.19	1.07 ± 0.47	0.49	2
4660	6.80 ± 0.23	12.55 ± 2.05	192 ± 3	145 ± 14	2.97 ± 0.41	1.12 ± 0.15	0.13	2
5982	6.24 ± 0.07	8.90 ± 0.90	242 ± 4	46 ± 26	2.60 ± 0.60	1.06 ± 0.25	0.48	1

Note. — Column (1): NGC number of galaxy. Column (2): $(FUV-V)_0$ in AB mag from [Bureau et al. \(2011\)](#). Column (3): age in Gyr from [Kuntschner et al. \(2010\)](#). Column (4): central velocity dispersion in km s⁻¹ from LEDA. Column (5): maximum rotation velocity in km s⁻¹ from LEDA. Column (6): specific frequency of GCs. Column (7): specific frequency per unit z-band luminosity (see Equation 1). Column (8): fraction of red GCs. Column (9): reference of GC data (1 = [Sikkema et al. 2006](#), 2 = [Peng et al. 2008](#)).

galaxies in the sample, and once for the galaxies with SSP-equivalent ages of ≥ 8 Gyr. This was done because the latter is thought to be the approximate age at which single EHB stars start producing the UV upturn feature as observed (e.g., [Chung et al. 2017](#)), and EHB stars are generally recognized to dominate the FUV luminosity of giant ETGs.

Focusing on panels (a), (b), (d), and (e) of Figure 1 (i.e., the stellar population parameters for the IUE sample), it can be seen that the well-known anticorrelation between $FUV-V$ and Mg₂ does not translate to a significant anticorrelation between $FUV-V$ and [Z/H] when taking all galaxies into account. However, the main outliers in this relation all have SSP-equivalent ages < 8 Gyr and high [Z/H], and $FUV-V$ does anticorrelate with [Z/H] when considering only the galaxies with ≥ 8 Gyr. Panel (e) reveals a significant anticorrelation between $FUV-V$ and SSP-equivalent age when considering all galaxies; however, this relation seems to be largely driven by the galaxies with ages < 8 Gyr, since the correlation weakens quite significantly when only considering the older galaxies. In this context, we remind the reader that the determinations of SSP-equivalent age of galaxies employed here are based on luminosity-weighted measurements of line indices in the blue and visual parts of the spectrum. Such age measurements are quite sensitive to the presence of young populations with small mass fractions (e.g., [Thomas et al. 2003](#)). As such, SSP-

equivalent ages of galaxies formally measure lower limits to the average age. Finally, the anticorrelation between $FUV-V$ and [α /Fe] shown in panel (d) is stronger than those between $FUV-V$ and either [Z/H] or SSP age. This suggests that, among the stellar population parameters, [α /Fe] seems to be the strongest driver of the $FUV-V$ vs. Mg₂ anticorrelation, even though it seems probable that [Z/H] and age also have some influence. Panel (c) of Figure 1 shows the well-known strong anticorrelation of $FUV-V$ with central velocity dispersion, and hence with the depth of the potential well of the galaxy (and the surrounding galaxy group or cluster if present).

The trends and anticorrelations mentioned above are generally consistent with those found by other recent studies of the UV upturn among ETGs (e.g., [Bureau et al. 2011](#); [Carter et al. 2011](#); [Jeong et al. 2012](#); [Smith et al. 2012a](#)), except that the anticorrelations found in the current paper are typically stronger than those in the other studies. We suggest that this may be due to the FUV emission in ETGs being more centrally concentrated than the V-band light ([Ohl et al. 1998](#); [Carter et al. 2011](#)). Thus, smaller measurement apertures in conjunction with aperture matching between measurements of the various population properties are likely to reveal stronger correlations between $FUV-V$ and other parameters. The IUE measurements were made through an aperture of $10'' \times 20''$ which corresponds to a (circularized) radius in the approximate

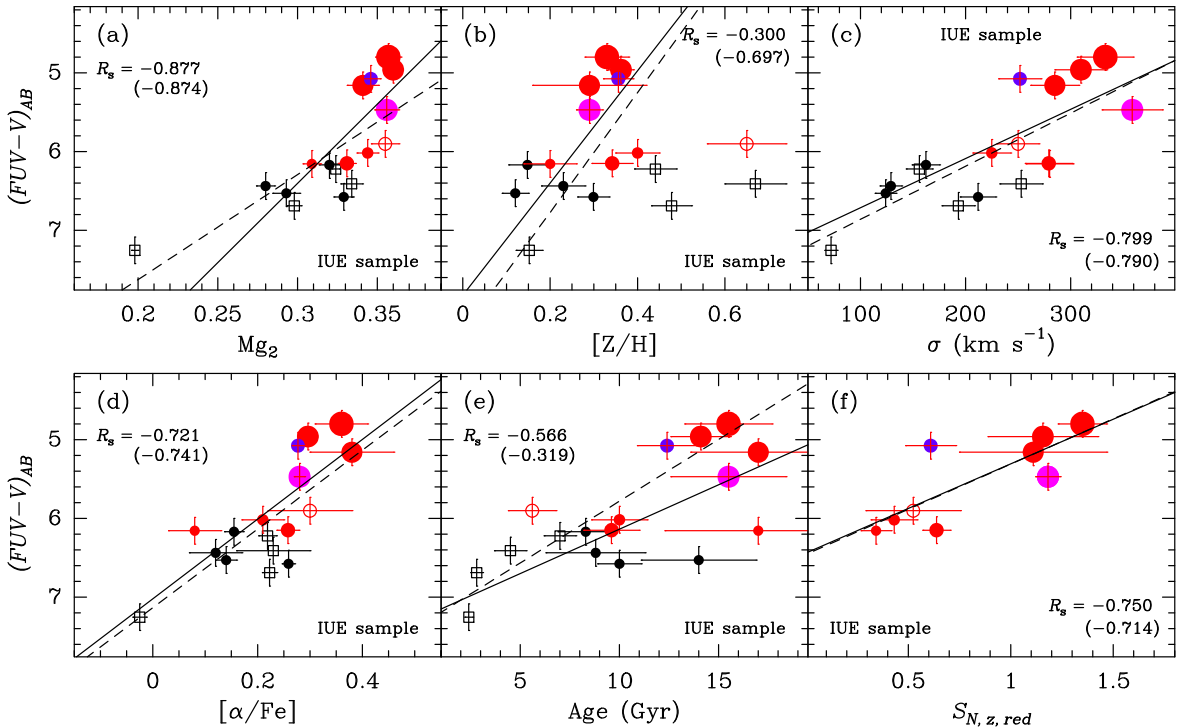


Figure 1. Correlations between $FUV-V$ and galaxy properties for the IUE sample. Panel (a): $FUV-V$ vs. Mg_2 . Panel (b): $FUV-V$ vs. $[Z/H]$. Panel (c): $FUV-V$ vs. central velocity dispersion. Panel (d): $FUV-V$ vs. $[\alpha/Fe]$. Panel (e): $FUV-V$ vs. age. Panel (f): $FUV-V$ vs. $S_{N,z,red}$, the specific frequency of metal-rich GCs. In each panel, red, purple, or magenta symbols refer to galaxies for which $S_{N,z,red}$ is available; the size of those symbols scales linearly with the value of $S_{N,z,red}$. The purple symbol indicates NGC 4552, a galaxy with a LINER nucleus emitting part of its FUV luminosity. The magenta symbol indicates NGC 4889, a Coma elliptical whose distance is $\gtrsim 4$ times larger than that of all other galaxies in this sample. Open symbols refer to galaxies with SSP-equivalent ages ≤ 8 Gyr, while filled symbols refer to older galaxies. The Spearman rank correlation coefficient R_s is mentioned in each panel for the relation in question, both for all galaxies and for galaxies with SSP-equivalent ages > 8 Gyr (the latter in parentheses). Linear least-square fits to the data are shown in each panel by dashed lines (for all galaxies) and solid lines (for galaxies with SSP ages > 8 Gyr). See discussion in Sect. 3.

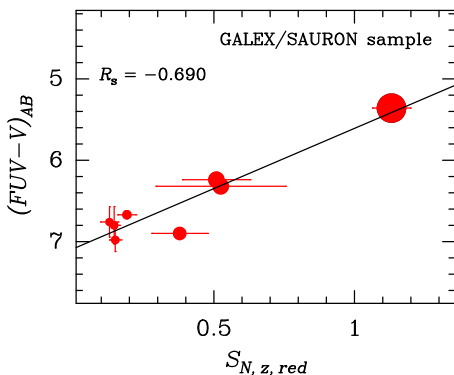


Figure 2. Same as panel (f) of Figure 1, but now for the SAURON sample.

range $R_{\text{eff}}/8$ to $R_{\text{eff}}/4$ for most galaxies in the IUE sample⁶ (see, e.g., Caon et al. 1993; Goudfrooij et al. 1994a). In contrast, the studies of the UV upturn in the SAURON sample (Bureau et al. 2011; Jeong et al. 2012) used measurements of $FUV-V$ within an aperture of $R_{\text{eff}}/2$ for their correlation analysis, so that the influence of the FUV-emitting population can be expected to be somewhat diluted relative to the $FUV-V$ measurements of galaxies in the IUE sample.

A new relation found here is that $FUV-V$ anticorrelates strongly with $S_{N,z,red}$, the specific frequency of metal-rich GCs. This is shown in panel (f) of Figure 1 for the IUE sample, and in Figure 2 for the SAURON sample. The nature

⁶ NGC 4889 is an exception due to its distance being $\gtrsim 4$ times larger than that of all other galaxies in the IUE sample. Hence it is assigned a different symbol in Figure 1.

and possible implications of this relation are discussed in the next section.

4. GCS AS A SOURCE OF FAR-UV FLUX IN GALACTIC SPHEROIDS

The anticorrelation of $FUV-V$ with $S_{N,z,red}$ reported here could in principle simply reflect the already known anticorrelation between $FUV-V$ and σ in conjunction with the correlation between M_V and $S_{N,z,red}$ reported by Peng et al. (2008) for galaxies in the Virgo cluster with $M_z \lesssim -21$. However, the correlation between $FUV-V$ and $S_{N,z,red}$ is stronger than that between M_V and $S_{N,z,red}$. Furthermore, panels (a)–(e) of Figure 1 show that galaxies with the highest values of $S_{N,z,red}$ systematically have bluer $FUV-V$ colors than that indicated by the linear fits to the relations shown by the lines in each panel. At face value, this seems to suggest that $S_{N,z,red}$ has a causal anticorrelation with $FUV-V$. With this in mind, we consider the hypothesis that the He-enhanced populations that are likely responsible for the UV upturn are produced in massive star clusters and subsequently disperse slowly into the field population of galaxies by means of dissolution of metal-rich GCs in the strong tidal field within the inner regions of luminous ETGs. This hypothesis is explored below.

4.1. Long-term Dissolution of Metal-Rich GCs

4.1.1. Empirical Evidence

First, we describe empirical evidence for significant amounts of mass loss from metal-rich GCs in the central regions of massive ETGs. Several studies of GC systems around ETGs have shown that surface number density profiles of metal-rich GCs outside $\sim 1 R_{\text{eff}}$ typically follow the surface brightness profile

of the host galaxy, while the metal-poor GCs have a much shallower profile (e.g., Geisler et al. 1996; Forbes et al. 1998; Rhode & Zepf 2004; Dirsch et al. 2005; Bassino et al. 2006; Harris et al. 2010; Strader et al. 2011). As such, metal-rich GCs are thought to be physically associated with the luminous component of the galaxies (“bulge”), while the metal-poor GCs are more of a “halo”-like population. Recent studies of nearby ETGs have shown that this difference in radial distribution between metal-rich and metal-poor populations is shared by the field stars (Harris et al. 2007; Rejkuba et al. 2014; Peacock et al. 2015). In fact, these studies found the fraction of metal-poor field stars in the inner regions of ETGs to be even lower than one would predict based on the difference in radial number density profiles between metal-rich and metal-poor GCs mentioned above.

However, *HST* studies of “normal,” old ETGs have shown that the surface number densities of metal-rich GCs are significantly depleted in the central regions relative to the galaxy light profile (e.g., Forbes et al. 2006; Peng et al. 2006; Harris et al. 2017). Interestingly, this depletion is much weaker for early-type merger remnant galaxies such as NGC 1316 (Goudfrooij et al. 2001) and NGC 3610 (Goudfrooij et al. 2007), which are only a few Gyr old, so that dynamical evolution of GCs has had much less time to disperse their stars into the field. It thus seems fair to suggest that these depletions of the surface number densities of metal-rich GCs toward the galaxy centers are due to dynamical evolution (two-body relaxation (or “evaporation”) and tidal shocking) in the central regions.

4.1.2. Quantitative Estimates

To estimate the amount of GC mass loss occurring in the inner regions of ETGs, we proceed as follows. We assume that GCs are tidally limited, meaning that their average mass densities are determined by the galaxy density inside their orbits (e.g., King 1962). For simplicity, we assume circular orbits, and we follow Fall & Zhang (2001) by relating the mass densities of GCs to their galactocentric radius R_{gal} in a steady-state isothermal potential $\Phi(R_{\text{gal}}) = V_{\text{gal}}^2 \ln(R_{\text{gal}})$ with a fixed maximum velocity $V_{\text{gal}} = (V^2 + \sigma^2)^{1/2}$ where V is the galaxy’s maximum rotational velocity and σ is its central velocity dispersion. In this case, the mean evaporative mass loss rate μ_{ev} of a cluster is given by

$$\mu_{\text{ev}} \approx 2.9 \times 10^4 \left(\frac{R_{\text{gal}}}{\text{kpc}} \right)^{-1} \left(\frac{V_{\text{gal}}}{220 \text{ km s}^{-1}} \right) M_{\odot} \text{ Gyr}^{-1} \quad (2)$$

(see Equations (4) and (15) in Fall & Zhang 2001). It should be emphasized that μ_{ev} in Equation (2) likely represents a lower limit to the actual average mass loss rate of surviving metal-rich GCs since their birth. Under the assumption that metal-rich GCs were formed in situ during the star-forming era of massive building blocks of present-time giant ETGs, it is likely that disruption rates of GCs in such dense environments at high redshift were significantly higher than they are currently, due to the stronger tidal perturbations (this may especially be the case for the metal-rich GCs, see Kruijssen 2015). Furthermore, application of Equation (2) neglects early mass loss by processes such as residual gas expulsion (Baumgardt et al. 2008) and ejection of stars from the cluster as it expands adiabatically after the death of the massive stars in the cluster (Hills 1980). The rate of the latter type of mass loss is strongly dependent on the level of primordial mass segregation of the cluster (e.g., Vesperini et al. 2009).

4.2. Comparison with Radial Number Density Distributions

We compare the mass lost from GCs as a function of galactocentric radius as described above with the radial number density distributions of metal-rich GCs for six giant ETGs from the ACS Virgo Cluster Survey (ACSVCS; Côté et al. 2004; Jordán et al. 2009). These galaxies were selected for hosting GCs whose $g - z$ color distribution clearly shows two distinct peaks, facilitating a simple distinction between metal-poor and metal-rich GCs (see Goudfrooij & Kruijssen 2013 for the exact selection criteria). Four of these galaxies are in the IUE sample described in Section 3, while the other two (NGC 4473 and NGC 4486 = M87) are in the SAURON sample. Radial distributions of surface number densities of metal-rich GCs in these galaxies were derived from the tables in Jordán et al. (2009) as follows. GCs were first defined as sources to which $p_{\text{GC}} \geq 0.5$. To avoid incompleteness-related issues, we considered only GCs with $z \leq 22.9$, corresponding to the 90% completeness limit in the inner regions of the host galaxy with the highest central surface brightness. Completeness-corrected numbers of metal-rich GCs, N_{GC} , were determined in annuli with logarithmic spacing in galactocentric radius. These N_{GC} values were then divided by the area of the annuli, taking into account the limited azimuthal coverage of the outermost annuli. Figure 3 shows the surface number density distributions of the metal-rich GCs in these galaxies, along with the surface brightness profiles of the parent galaxy and the average amount of mass lost from GCs as a function of galactocentric radius during a time span of 12 Gyr according to Equation (2) for comparison purposes. Note that the surface number density profiles of metal-rich GCs flatten out significantly (relative to the surface brightness profile of the parent galaxy) inside $R_{\text{gal}} \approx 30''$ of these galaxies, corresponding to ≈ 2.5 kpc at the distance of the Virgo cluster (16.5 Mpc, see Jordán et al. 2009), where the typical evaporative mass lost from GCs over 12 Gyr according to Equation (2) (hereafter referred to as Δ_{GC}) is of order $2 \times 10^5 M_{\odot}$. Furthermore, the level of depletion of the surface number densities of metal-rich GCs relative to the galaxy light increases toward smaller R_{gal} . This is consistent with the fact that Δ_{GC} increases to $10^6 M_{\odot}$ or beyond in those innermost regions: only the GCs with the highest initial masses have been able to survive dissolution by the strong tidal forces in those regions until the present time.

5. FEASIBILITY OF PROPOSED SCENARIO

5.1. Energetics

In this section we evaluate the feasibility of the hypothesis that He-rich EHB stars associated with (now mostly dissolved) massive metal-rich GCs can indeed produce the observed range of $FUV - V$ among giant ETGs. To do so, we use the observational results of the FUV emission of massive GCs in M87 from Sohn et al. (2006).

5.1.1. Required Numbers of GCs

We first make the assumption that the FUV properties of the surviving metal-rich GCs constitute a suitable proxy for the GCs that dissolved over the last several Gyr. Since it is likely that the initial masses of the dissolved GCs were on average lower than those of the surviving GCs (at a given tidal field strength and evaporation rate, that is), the implicit assumption is that the dependence of $FUV - V$ on GC mass is small within the applicable range of GC masses. To assess the validity of this assumption, we plot $FUV - V$ versus M_{γ}

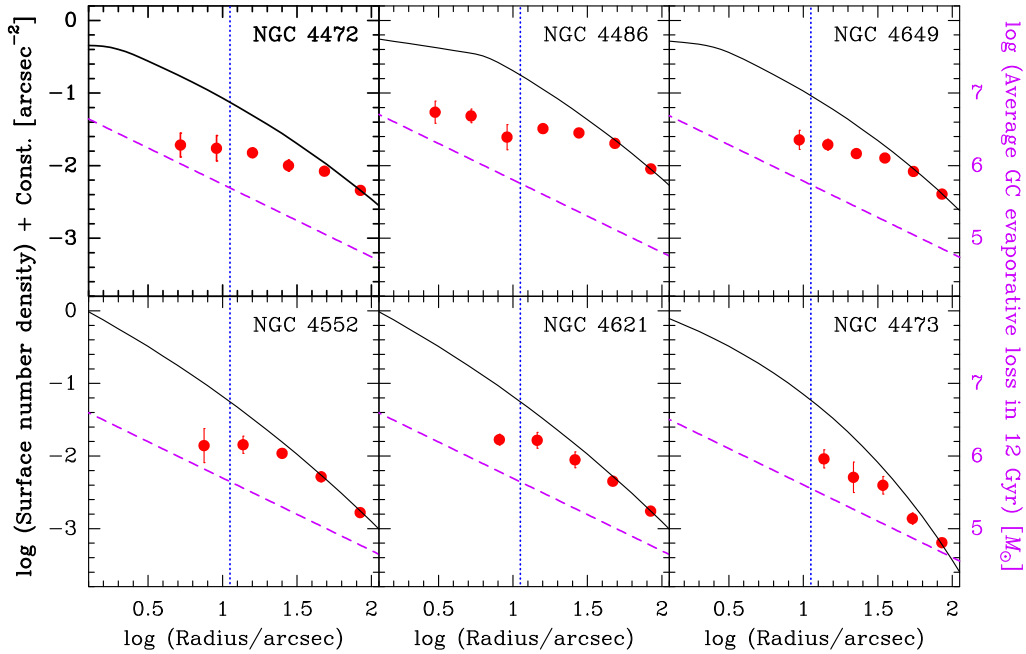


Figure 3. Radial surface number density profiles for the metal-rich GCs in six giant ETGs in the Virgo cluster of galaxies from *HST*/ACS data. The galaxy names are indicated at the top right of each panel. Surface number density data were derived as explained in the text, and are shown as open circles. The solid lines represent the surface brightness profiles of the integrated z -band light of the galaxies (taken from Ferrarese et al. 2006), normalized to agree with the value of the outermost GC number density. The purple dashed lines represent the logarithm of the average mass accumulated by evaporation of GCs over a time span of 12 Gyr as a function of galactocentric radius according to Equation (2), for which the scale is shown on the right-hand side of the figure. For comparison purposes, the circularized radius of the IUE measurement aperture is indicated by vertical blue dotted lines. See discussion in Section 4.2.

for the M87 GCs from Sohn et al. (2006) in Figure 4.7 To discriminate between metal-poor and metal-rich GCs in this context, we adopt the color threshold $V-I = 1.09$ as determined by Kundu et al. (1999) whose *HST*/WFPC2 photometry was used by Sohn et al. (2006) as well. Current GC mass estimates are indicated in Figure 4, assuming a typical $M/L_V = 1.8$ (Goudfrooij & Fall 2016; Harris et al. 2017). Note that there is no significant mass dependence of $FUV-V$ for GCs with $M_V \lesssim -8.0$, corresponding to $M \gtrsim 2 \times 10^5 M_\odot$. This is the case for both the metal-poor and the metal-rich GCs. As such, the following calculations pertain to GCs with current masses $M \gtrsim 2 \times 10^5 M_\odot$. Among these massive metal-rich GCs in M87, we find a mean $M_V^0 = -9.64$, corresponding to a mean mass $M \sim 1 \times 10^6 M_\odot$. Their mean $FUV-V = 4.82$ in AB mag, corresponding to $M_{FUV}^0 = -4.82$ in AB mag at the distance of the Virgo cluster.

A second assumption we make is that single He-rich EHB stars created in massive GCs are unlikely to be the *only* source of FUV luminosity in ETGs. For instance, the model of Han et al. (2007), i.e., hot helium-burning stars that have lost their hydrogen-rich envelopes in binary interactions (be it in GCs or in the field), may well provide a *minimum* strength of the UV upturn (or maximum $FUV-V$, hereafter $(FUV-V)_{\max}$) in ETGs. The model of Han et al. predicts $(FUV-V)_{\max}$ in the range 6.5 – 7.0 (with the precise value depending on the parameter values of the model), with a negligible dependence on age for ages $\gtrsim 1$ Gyr. Interestingly, this range of $(FUV-V)_{\max}$ is roughly consistent with the maximum value of $FUV-V$ seen in samples of ETGs (see Figure 1; Bureau et al. 2011; Jeong et al. 2012). With this in mind, we explore to what extent the *range* in $FUV-V$ seen among ETGs can be understood in terms of GC formation efficiencies and dynamical evolution

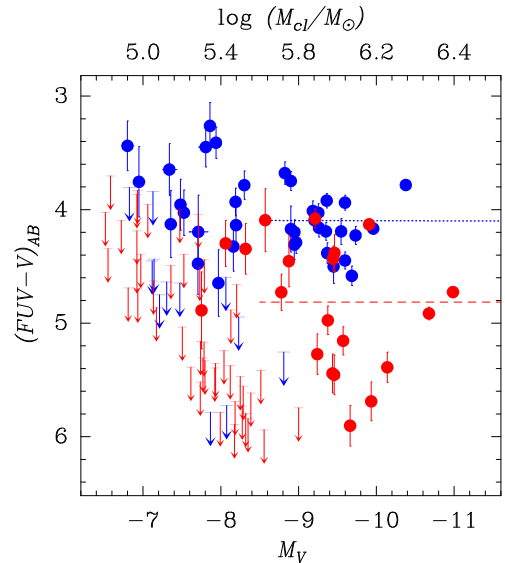


Figure 4. $(FUV-V)_{AB}$ versus M_V for GCs in M87 from Sohn et al. (2006). Blue symbols indicate metal-poor GCs and red symbols indicate metal-rich GCs. FUV upper limits are indicated by downwards arrows. The blue dotted line and red dashed line represent linear least-square fits to the metal-poor and metal-rich GCs with $M_V \leq -8.5$, respectively. Estimated GC masses are indicated along the top abscissa.

of massive GCs.

The range of UV upturn strengths among ETGs in $FUV-V$ is ~ 1.5 mag (see Figure 1; Bureau et al. 2011). Relevant ETGs representing the bottom and top of this range are NGC 4473 and NGC 4649, respectively.⁸ These two galaxies have the same SSP age to within the uncertainties as determined

⁷ Following Sohn et al. (2006), we use $(FUV-V)_{AB} = (FUV-V)_{STMAG} + 2.82$.

⁸ We exclude the strong UV upturns in NGC 1399 and M87 from this exercise, since their FUV emission is due in part to unresolved nuclear emission (Carter et al. 2011).

from their Lick indices (see Tables 1 and 2), suggesting that their production rates of EHB stars by stellar evolution are consistent with each other as well. Since NGC 4473 has $FUV-V = 6.90 \pm 0.06$ within $R_{\text{eff}}/2$ (Bureau et al. 2011), it constitutes a relevant example of an ETG for which a significant fraction of the FUV luminosity may be due to hot subdwarf stars produced in binary systems. To derive $FUV-V$ within $R_{\text{eff}}/2$ for NGC 4649, we download GALEX dataset G13_041008_NGC4621 from the [STScI/MAST GR6 archive](#), with an exposure time of 1658 s in the NUV and FUV passbands. This GALEX dataset is available at the MAST archive at doi.org/10.17909/T9V68G. Following Bureau et al. (2011), we carry out surface photometry of NGC 4649 using the ELIPSE task in [IRAF/STSDAS](#), using the NUV image to perform ellipse fitting followed by imposing those ellipses on the FUV image. For the sky background level we use the mean of unclipped mean values in 15 square apertures located around the galaxy, in regions free from stars or other galaxies. We adopt a photometric zero point of 18.82 mag (Morrissey et al. 2005), and correct the photometry for Galactic extinction using the E_{B-V} value from Schlegel et al. (1998) as mentioned in NED in conjunction with the extinction law of Cardelli et al. (1989). To obtain V -band photometry for NGC 4649, we use the B -band surface photometry tables of Peletier et al. (1990) in conjunction with the $B-V$ colors from Burstein et al. (1987), interpolating in galactocentric radius. Adopting $R_{\text{eff}} = 74''.3$ for NGC 4649 (Burstein et al. 1987), we obtain $M_{FUV, AB}^0 = -15.50$, $M_V^0 = -21.01$, and $FUV-V = 5.51$ within $R_{\text{eff}}/2$, i.e., 1.39 mag bluer in $FUV-V$ than NGC 4473.

To determine how many ‘‘average’’ FUV-bright massive metal-rich GCs as seen in M87 are needed to produce the ‘‘extra’’ FUV luminosity in NGC 4649 relative to NGC 4473, we iteratively add such GCs (for which $M_V^0 = -9.64$ and $M_{FUV}^0 = -4.82$, see above) to NGC 4473 and re-evaluate its integrated M_V and M_{FUV} until we produce a galaxy with $FUV-V = 5.51$. We find that this would require 7789 such GCs. These would produce $M_V = -19.41$, which is 1.60 mag fainter than the actual light within $R_{\text{eff}}/2$ in NGC 4649, equivalent to a V -band luminosity fraction $f_V = 0.23$.

In conclusion, the range in $FUV-V$ seen among ETGs can be produced by (currently largely dissolved) FUV-bright GCs similar to those seen in M87 with numbers of such GCs that produce V -band luminosity fractions up to $f_V \sim 0.23$.

5.1.2. Consistency with GC Mass Loss Scenario

One might wonder whether this range of f_V is consistent with that expected from GC mass loss over a time span similar to the age of such galaxies (for which we adopt 12 Gyr as before). To address this question, we use the semi-analytical dynamical evolution model of Goudfrooij & Fall (2016). As commonly done in star cluster evolution modeling, we adopt a Schechter (1976) function for the initial cluster mass function (ICMF):

$$\psi_0(M_0) = A M_0^\beta \exp(-M_0/M_c), \quad (3)$$

where M_0 is the initial cluster mass, and the adjustable parameters are A , β , and M_c . The ICMF has a power-law shape with exponent $\beta = -2$ below M_c to mimic the observed mass functions (MFs) of young cluster systems (e.g., Zhang & Fall 1999; Chandar et al. 2010; Portegies Zwart et al. 2010; Whitmore et al. 2014), and it has an exponential decline above the ‘‘characteristic truncation

mass’’ M_c as suggested by the observed tail of the GC mass function (GCMF) at $M \gtrsim 10^6 M_\odot$ for GC systems in ancient galaxies. Following Goudfrooij & Fall (2016), we incorporate mass loss by stellar evolution based on the BC03 models and we make the common assumption that the long-term dynamical mass loss of GCs is dominated by two-body relaxation (see also, e.g., Gnedin & Ostriker 1997; Dinescu et al. 1999; Kruijssen 2015). In that case, the evolving GCMF at time t is

$$\psi(M, t) = A M^{\gamma-1} (M^\gamma + \mu_{\text{ev}} t)^{(\beta-\gamma+1)/\gamma} \times \exp\left[-(M^\gamma + \mu_{\text{ev}} t)^{1/\gamma}/M_c\right] \quad (4)$$

(Goudfrooij & Fall 2016) where μ_{ev} is the evaporative mass loss rate (cf. Equation 2) and $\gamma \leq 1$ denotes the exponential dependence of the dissolution time on GC mass (i.e., $t_{\text{dis}} \propto M^\gamma$). $\gamma = 1$ for classical two-body relaxation as defined by Spitzer (1987) and others. While the actual value of γ is currently not well constrained for GCs with $M \gtrsim 10^5 M_\odot$ after a Hubble time of dynamical evolution (see discussion in Goudfrooij & Fall 2016), the main effect of $\gamma < 1$ in the context of this study is that it yields slightly lower mass loss rates for low-mass clusters (i.e., GCs with $M < \mu_{\text{ev}} t$) relative to the case of $\gamma = 1$.⁹ To maximize the mass loss rate for low-mass GCs relative to high-mass GCs, we choose $\gamma = 1$. As such, the values for f_V calculated below formally represent lower limits.

To convert f_V to a mass fraction f_{GC} at $t = 12$ Gyr, we assume a GC mass-independent $M/L_V = 1.8 M_\odot/L_{V, \odot}$, which is a good approximation to dynamical M/L_V values determined by various studies of stellar kinematics in GCs (see Goudfrooij & Fall 2016, Harris et al. 2017, and references therein). We then determine f_{GC} for GCs above a given initial mass M_{limit} by integrating the ICMF (i.e., Equation 3) as well as Equation (4) for $t = 12$ Gyr and evaluating the difference. This procedure is illustrated in Figure 5. This evaluation is done for several values of M_{limit} while varying μ_{ev} and M_c within ranges typically found among GCMF studies of massive galaxies ($4.0 \leq \log(\mu_{\text{ev}}/(M_\odot \text{ Gyr}^{-1})) \leq 5.5$ and $6.0 \leq M_c/M_\odot \leq 7.5$, see Jordán et al. 2007; McLaughlin & Fall 2008; Chandar et al. 2010; Bastian et al. 2012; Goudfrooij & Fall 2016; Johnson et al. 2017).

For the low-mass truncation of the power-law tail of the ICMF, many studies use $M_{0, \text{min}} = 10^2 M_\odot$ which corresponds to the approximate minimum mass of a cluster for which the evaporation time scale is 10^8 yr, the typical lifetime of open clusters in the solar neighborhood (Adams & Myers 2001; Lada & Lada 2003). However, metal-rich GCs in giant ETGs are generally thought to have formed in high-pressure environments similar to those seen in vigorously star-forming galaxies at high redshift (e.g., Ashman & Zepf 1992; Kruijssen 2015) where SFRs exceed $10^2 M_\odot \text{ yr}^{-1}$ and turbulent velocities are of order $\sigma = 10 - 100 \text{ km s}^{-1}$ (Law et al. 2009, 2012; Genzel et al. 2010; Tacconi et al. 2013). In such harsh environments, the crossing time of a (proto)cluster with a typical half-mass radius $r_h \sim 1 \text{ pc}$ is only of order $\tau_{\text{cross}} = r_h/\sigma = 10^4 - 10^5 \text{ yr}$, which is 1–2 orders of magnitude shorter than in the solar neighborhood. Fokker-Planck modeling of GCs suggests that the evaporation time of a multi-mass cluster is of order $\tau_{\text{ev}} \approx 10 \tau_{\text{rel}}$ where τ_{rel} is the

⁹ This effect is not detectable in observations because the lower mass loss rates for those low-mass GCs result in higher M/L ratios, and the two effects cancel out in luminosity functions (Goudfrooij & Fall 2016).

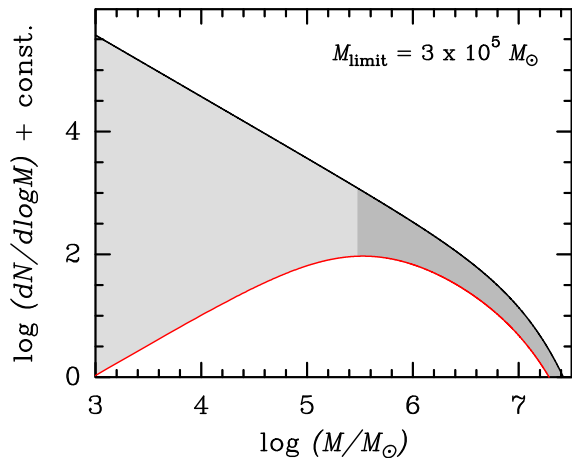


Figure 5. Example illustration of the determination of f_{GC} , the fraction of mass lost from GCs with initial masses above a certain mass limit M_{limit} over a time span of 12 Gyr. The black solid line represents the ICMF (i.e., Equation 3) using $M_c = 10^7 M_\odot$, while the red solid line depicts the GCMF after $t = 12$ Gyr of dynamical evolution (Equation 4 with $\gamma = 1$), using an evaporation rate $\mu_{\text{ev}} = 3 \times 10^4 M_\odot \text{Gyr}^{-1}$. The hashed region indicates the amount of mass lost by dynamical evolution over 12 Gyr, while the darker gray part of that region indicates the fraction of mass lost from GCs with initial masses $M_0 \geq M_{\text{limit}} = 3 \times 10^5 M_\odot$. See discussion in Section 5.1.2.

half-mass relaxation time of the cluster (e.g., Lee & Goodman 1995). Since $\tau_{\text{rel}}/\tau_{\text{cross}} \sim 0.1 N/\ln N$ where N is the number of stars in the cluster (Binney & Tremaine 1987), it follows that for a cluster to survive evaporation over a star formation time scale of 10^7 yr in such high-pressure environments, the requirement is $0.1 N/\ln N \gtrsim 10 - 100$, corresponding to $N \gtrsim 1500 - 5000$ cluster stars. With this in mind, we perform calculations of f_{GC} with $10^2 \leq M_{0,\text{min}}/M_\odot \leq 10^4$. Results are shown in Figure 6. Panels (a)–(c) plot f_{GC} versus M_{limit} , while panels (d)–(f) plot Δf_{GC} versus M_{limit} , where $\Delta f_{GC} \equiv f_{GC}(M_{\text{limit}}, M_c, \mu_{\text{ev}}) - f_{GC}(M_{\text{limit}}, 10^6 M_\odot, 10^4 M_\odot \text{Gyr}^{-1})$, i.e., the value of f_{GC} relative to that for $M_c = 10^6 M_\odot$ and $\mu_{\text{ev}} = 10^4 M_\odot \text{Gyr}^{-1}$.

Note that the range of Δf_{GC} implied by the hypothesis that the range of $FUV-V$ seen among ETGs is produced by (now largely dissolved) massive metal-rich GCs in the inner regions can indeed be reproduced by dynamical evolution of such GCs under quite reasonable conditions. Specifically, we find that the range $\Delta f_{GC} \lesssim 0.23$ (cf. Section 5.1.1) is covered if M_c is in the range $10^6 \lesssim M_c/M_\odot \lesssim 10^7$. Encouragingly, this range of M_c implied by our hypothesis is *entirely consistent with results of fits of Equation (4) (for $\gamma = 1$) to observed GC luminosity functions (GCLFs) of giant ETGs*, for which M_c is found to increase with ETG luminosity and hence presumably also ETG mass (Jordán et al. 2007; Johnson et al. 2017)¹⁰. Generally, Figure 6 shows that f_{GC} for ETGs with the weakest UV upturns is reached for low values for M_c and/or μ_{ev} , while f_{GC} values for strong UV upturns require higher values for M_c and/or μ_{ev} .

Summarizing this section, we find that the range of observed $FUV-V$ colors in the inner regions of nearby ETGs is consistent with our hypothesis that the range in $FUV-V$ seen among ETGs is produced by He-rich EHB stars associated with massive ($\log(M_0/M_\odot) \gtrsim 5.5$) metal-rich GCs, most of which have dissolved after ~ 12 Gyr of dynamical evolution. The $FUV-V$ colors of ETGs with the weakest UV

upturns and low values of S_N are consistent with GCs that were formed in environments featuring relatively low SFRs, associated with relatively low characteristic truncation masses ($M_c \approx 10^6 M_\odot$), whereas the GCs in ETGs with the strongest UV upturns and high S_N values were likely formed in vigorously star-forming environments where $M_c \approx 10^7 M_\odot$. This result is supported by the recent numerical simulations of GC formation at high redshift by Li et al. (2017), who found a correlation between M_c and SFRs such that $M_c \propto \text{SFR}^{1.6}$.

5.1.3. The Connection between M_c and S_N

While the previous section clarified that the range of f_{GC} implied by the observed range of $FUV-V$ among ETGs in the context of our hypothesis can be explained by a range in M_c among ETGs similar to that observed, it does not directly explain how the observed anticorrelation between $FUV-V$ and S_N seen in Figures 1 and 2 fits in with this scenario. This is addressed in this section.

Following the original definition of the specific frequency of GCs by Harris & van den Bergh (1981), S_N values are determined by parameterizing the observed completeness-corrected GCLF as a Gaussian in magnitude units. After fitting the turnover magnitude M_{T0} of the Gaussian, the total number of GCs is determined by counting the number of GCs brighter than M_{T0} and doubling that value. (The reason behind this methodology is to avoid incompleteness-related issues at faint magnitudes.)

In the presence of a range of M_c among GCMFs of ETGs where M_c increases with galaxy luminosity and mass, it is instructive to test the sensitivity of S_N to M_c , because the latter affects the width of the GCLF at old age. This is illustrated in panel (a) of Figure 7, while we plot S_N as a function of $\log M_c$ at an age of 12 Gyr in panel (b) of Figure 7. These values of S_N were derived by evaluating Equation (4) for $\gamma = 1$, $\mu_{\text{ev}} = 3 \times 10^4 M_\odot \text{Gyr}^{-1}$, $t = 12$ Gyr, and a range of $\log M_c$. Note that the aforementioned estimated range $10^6 \lesssim M_c/M_\odot \lesssim 10^7$ for ETGs with UV upturns implies a range in S_N of a factor ~ 1.7 , which is similar to the range in $S_{N,z,\text{red}}$ actually found among the galaxies in our sample (see Figures 1(f) and 2).

We thus arrive at a picture where the observed ranges of both $FUV-V$ and $S_{N,z,\text{red}}$ can be largely explained by the observed range in M_c , which in turn can be explained by a range of SFR (or SFR surface density, see also Johnson et al. 2017) occurring in the progenitors of the present-day ETGs, with the more massive ETGs containing higher mass fractions from more massive protogalaxies, which formed their stars earlier and with higher SFRs than the less massive ones.

5.2. Metallicities of Metal-rich GCs and the Underlying Field Population

As to the actual metallicities of the metal-rich GCs in the FUV -emitting (inner) regions of ETGs, it has been suggested that they are typically lower than that indicated by the underlying diffuse light of the parent galaxy (e.g., Peng et al. 2006; Sohn et al. 2006), thus casting some apparent doubt on whether these GCs might be able to explain the UV upturns in ETGs through the scenario advocated here. However, we emphasize that metallicity data on GCs in the inner regions of ETGs (including M87) are virtually always based on optical photometry rather than spectroscopy.¹¹ As shown by

¹⁰ Note that the values for M_c in Jordán et al. (2007) do not account for mass loss due to stellar evolution; the ones in Johnson et al. (2017) do.

¹¹ This is due to signal-to-noise constraints imposed by the high background level in the central regions of ETGs.

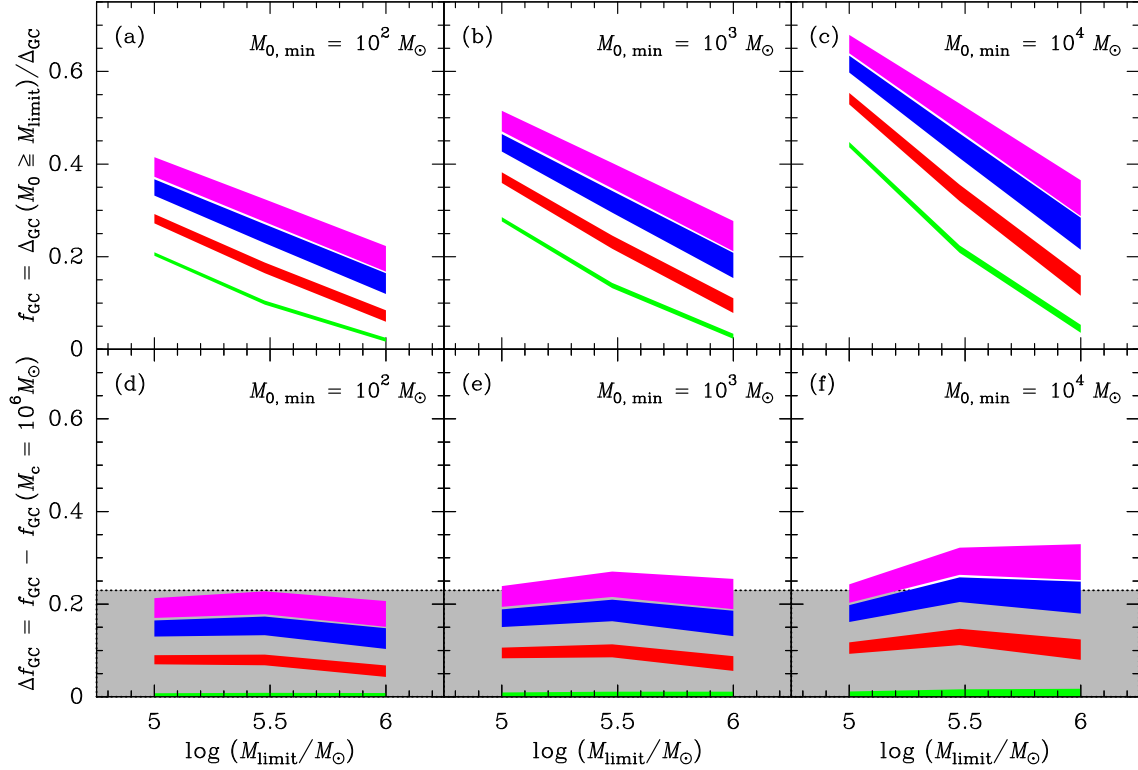


Figure 6. *Top panels:* f_{GC} versus M_{limit} . The colored regions in each panel show results obtained by numerically integrating Equations (3) and (4) for $4.0 \leq \log(\mu_{\text{ev}}/(M_{\odot} \text{Gyr}^{-1})) \leq 5.5$ and different values of M_c . Green regions represent $\log(M_c/M_{\odot}) = 6.0$, red regions represent $\log(M_c/M_{\odot}) = 6.5$, blue regions represent $\log(M_c/M_{\odot}) = 7.0$, and magenta regions represent $\log(M_c/M_{\odot}) = 7.5$. The different panels indicate different assumptions for the low-mass truncation of the ICMF, as indicated at the top right of each panel. *Bottom panels:* Δf_{GC} versus M_{limit} . The gray region depicts the range of f_{GC} implied by the hypothesis that the range of $FUV-V$ seen among ETGs is caused by dissolution of massive metal-rich GCs in the inner regions, based on the FUV luminosities of M87 GCs by [Sohn et al. \(2006\)](#). See discussion in Section 5.1.2.

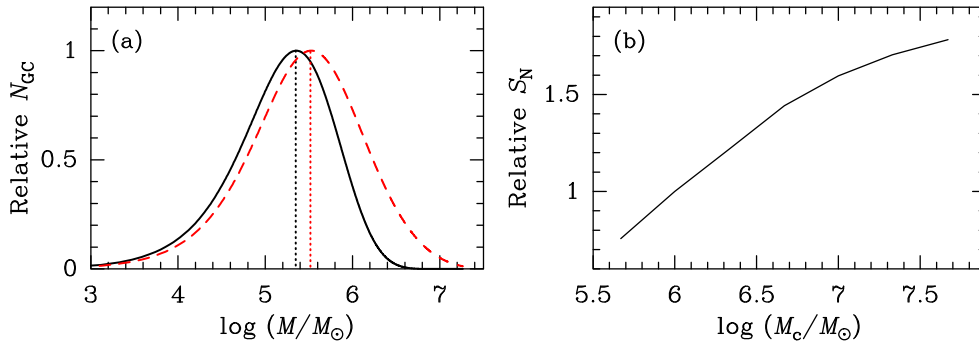


Figure 7. *Panel (a):* GCMFs (i.e., Equation 4) at $t = 12$ Gyr for $\mu_{\text{ev}} = 3 \times 10^4 M_{\odot} \text{Gyr}^{-1}$. The black solid line is for $M_c = 10^6 M_{\odot}$ while the red dashed line is for $M_c = 10^7 M_{\odot}$. For reference, the two vertical dashed lines indicate the values of the turnover mass for the two GCMFs. Note the significant difference in GCMF width between the two values of M_c . *Panel (b):* S_N versus M_c at $t = 12$ Gyr for $\mu_{\text{ev}} = 3 \times 10^4 M_{\odot} \text{Gyr}^{-1}$. Note that a range of M_c suggested by the discussion in Section 5.1.2 causes a range in S_N of a factor ~ 1.7 at a given evaporation rate.

[Goudfrooij & Kruijssen \(2013\)](#), the differences in optical colors between giant ETGs and their metal-rich GCs can be explained by differences in the stellar MFs. Specifically, several recent spectroscopic studies of giant ETGs have established evidence for bottom-heavy stellar MFs, with power-law slopes α in the sub-solar mass range that are at least as steep as that of the initial mass function (IMF) of [Salpeter \(1955\)](#), i.e., $-3.0 \lesssim \alpha \lesssim -2.3$ in $dN/dM \propto M^{\alpha}$ (e.g., [van Dokkum & Conroy 2010](#); [Conroy & van Dokkum 2012](#); [Smith et al. 2012b](#); [La Barbera et al. 2013](#); [McDermid et al. 2014](#); [Spiniello et al. 2014](#); [van Dokkum et al. 2017](#); [Sarzi et al. 2018](#)). For GCs that were born with such bottom-heavy IMFs, [Goudfrooij & Kruijssen \(2013\)](#) showed that 12 Gyr of dynam-

ical evolution causes the stellar MF of the average surviving (massive) GC to be similar to the canonical [Kroupa \(2001\)](#) IMF, thereby causing their optical colors to become bluer than the underlying field population by amounts similar to those observed (see also [Goudfrooij & Kruijssen 2014](#)). As such, the bluer colors of metal-rich GCs relative to their parent galaxies do not necessarily indicate differences in metallicity, which would indeed be unexpected under the common assumption that surviving GCs represent the high-mass end of the star formation processes that also created the field population ([Elmegreen & Efremov 1997](#)). Furthermore, in the few cases where high-quality spectroscopic Lick index data are available for both ETGs and their constituent GCs at com-

parable galactocentric distances, the metal-rich GCs have the same ages and metallicities as their parent ETGs to within small uncertainties (see [Goudfrooij & Kruijssen 2013](#) and references therein). This is also the case for M87, as detailed in the Appendix.

6. IMPLICATIONS OF THE PROPOSED SCENARIO

6.1. UV Upturn: Metal-poor and/or Metal-rich Populations?

Traditionally, the correlation of UV upturn strength with the Mg_2 index among ETGs has always been recognized as somewhat surprising, in the sense that the Galactic GCs with the strongest FUV fluxes are typically metal-poor (see, e.g., [Dorman et al. 1995](#); [O’Connell 1999](#)). One early scenario that was proposed to resolve this paradox postulated that the UV upturn was mainly produced by a minority ($\lesssim 20\%$) population of metal-poor stars ([Park & Lee 1997](#)), although this scenario required ages of $\gtrsim 16$ Gyr for the metal-poor component. More recently, the fact that the metal-poor GCs in M87 are on average brighter in the FUV than the metal-rich GCs (see [Sohn et al. 2006](#)) may have prompted [Chung et al. \(2011\)](#) to construct a model in which the fraction of helium-enhanced stars decreases with increasing metallicity, leading them to conclude that the bulk of the FUV flux in ETGs is produced by metal-poor (and He-rich) stars. While the model of [Chung et al. \(2011\)](#) produces a very good fit to the observed FUV upturn and optical SEDs of ETGs, it overproduces flux in the NUV (2000–3000 Å) region (see their Figure 3), which is consistent with a lack of metallicity-dependent line blanketing in the NUV in their model ([Dorman et al. 1995](#); [Tantalo et al. 1996](#)). Furthermore, the metallicity distribution of the FUV-bright population in the model of [Chung et al. \(2011\)](#) seems inconsistent with the observed anticorrelations between radial gradients of $FUV-V$ and metallicity within ETGs (both in Mgb and $[Z/H]$, [Jeong et al. 2012](#)), which are in the sense that UV upturn strength and metallicity both decrease with increasing galactocentric radius, while age does not. This suggests a physical association between UV upturn strength and metallicity.

In the context of the scenario described here, this physical association is implied by the differences in radial distribution and structural parameters between the metal-rich and the metal-poor GCs. The radial distributions of the two GC subpopulations in the central ~ 8 kpc of giant ETGs in the ACSVCS are shown in Figure 8, which is a copy of Figure 3 to which we added data points for the metal-poor GCs. Note that the surface number densities of metal-poor GCs in the inner regions are factors of 2–5 lower than those of the metal-rich GCs in ETGs with the strongest UV upturns such as M87 and NGC 4649. It is important to realize that this difference between the metal-poor and metal-rich GC systems in these galaxies is *not* due to differences in GC evaporation rates. First, as already mentioned in Section 4.1.1, the radial distribution of metal-rich GCs on larger radial scales (10–100 kpc) is consistent with that of the galaxy light whereas that of the metal-poor GCs is significantly more shallow. Secondly, the observed structural parameters of the GCs in these galaxies indicate that the evaporation rates of the metal-rich GCs are actually *higher* than those of the metal-poor GCs at a given projected R_{gal} . As shown by [Goudfrooij & Fall \(2016\)](#), the evaporation rate μ_{ev} of tidally limited GCs scales with their mass density as $\mu_{ev} \propto \rho_h^{1/2}$, where $\rho_h = 3M/(8\pi r_h^3)$ is the mean density of a GC within its half-mass radius (see also [McLaughlin & Fall 2008](#)). Figure 9 depicts the rolling mean

value of $\rho_h^{1/2}$ versus R_{gal} for the metal-poor and metal-rich GCs in the six ACSVCS galaxies also shown in Figure 8. Note that $\rho_h^{1/2}$ is systematically higher in metal-rich GCs than in metal-poor GCs. Statistically, the evaporation rate as measured by $\rho_h^{1/2}$ in metal-rich GCs is larger than that in metal-poor ones by a factor 1.32 ± 0.12 at a given R_{gal} among these six galaxies.

Even though the massive metal-poor GCs in M87 are brighter in the FUV than their metal-rich counterparts by a factor ~ 2 on average (see Figure 4), the metal-rich GCs have significantly higher surface number densities *as well as* higher evaporation rates than the metal-poor GCs in the central regions of the ETGs with the strongest UV upturns. It follows that the FUV emission is due mainly to metal-rich GCs in our scenario. This is consistent with the observed anticorrelations between radial gradients of $FUV-V$ and metallicity within ETGs as mentioned above.

6.2. Light-element Abundance Ratios in ETGs

If the scenario proposed here is correct, an important implication would be that the He-enhanced populations responsible for the UV upturn in ETGs would show light-element abundance ratios similar to those observed in massive GCs, i.e., enhancements in $[Na/Fe]$ and $[N/Fe]$ accompanied by (likely more metallicity-dependent, see [Ventura et al. 2013](#)) depletions of $[C/Fe]$ and $[O/Fe]$.

Specifically, the amplitude of light-element abundance variations in GCs is known to scale with GC mass (see Section 1), so that the largest such variations would be found in regions where the mass fraction of stars originating from massive GCs is highest. In the current scenario, that occurs where M_c and μ_{ev} are highest, i.e., the same regions where the UV upturn is strongest—the inner regions of ETGs, while the amplitude of these abundance variations would decrease toward the outer regions of ETGs. Interestingly, some recent spectroscopic studies do show evidence for this. Using stacked SDSS spectra of ETGs, [Schiavon \(2007\)](#) found a strong correlation between $[N/Fe]$ and galaxy luminosity, while [van Dokkum et al. \(2017\)](#) used deep spatially resolved spectroscopy of six ETGs and found that $[Na/Fe]$ increases toward the galaxy centers within $R_{gal} \lesssim R_{eff}/2$ (see also [Sarzi et al. 2018](#)), while $[O/Fe]$ decreases. These results are just as expected in the current scenario where the He enhancement is due to dissolution of massive GCs in the central regions. In this respect, a clear prediction from the current scenario is that future spectroscopic studies will also find radial gradients in $[N/Fe]$ that increase toward galaxy centers in massive ETGs, and that such radial gradients have the largest amplitudes in ETGs with the strongest UV upturns.

6.3. Interpretation of Correlations between UV Upturn and Galaxy Properties

If indeed the range of $FUV-V$ among ETGs is mainly caused by He-rich EHB stars that were formed in massive GCs, among which most were subsequently dissolved in the inner regions of giant ETGs, can we understand the previously known relations between $FUV-V$ and galaxy properties such as those shown in panels (a)–(e) of Figure 1?

First of all, the anticorrelation between $FUV-V$ and $[\alpha/Fe]$ can be understood, at least qualitatively, by the results of [Puzia et al. \(2006\)](#) who found that massive GCs in ETGs typically have very high $[\alpha/Fe]$ values, higher than those of the diffuse light of their parent galaxies. Hence, the higher the values of M_c and/or average μ_{ev} for a given ETG, the higher

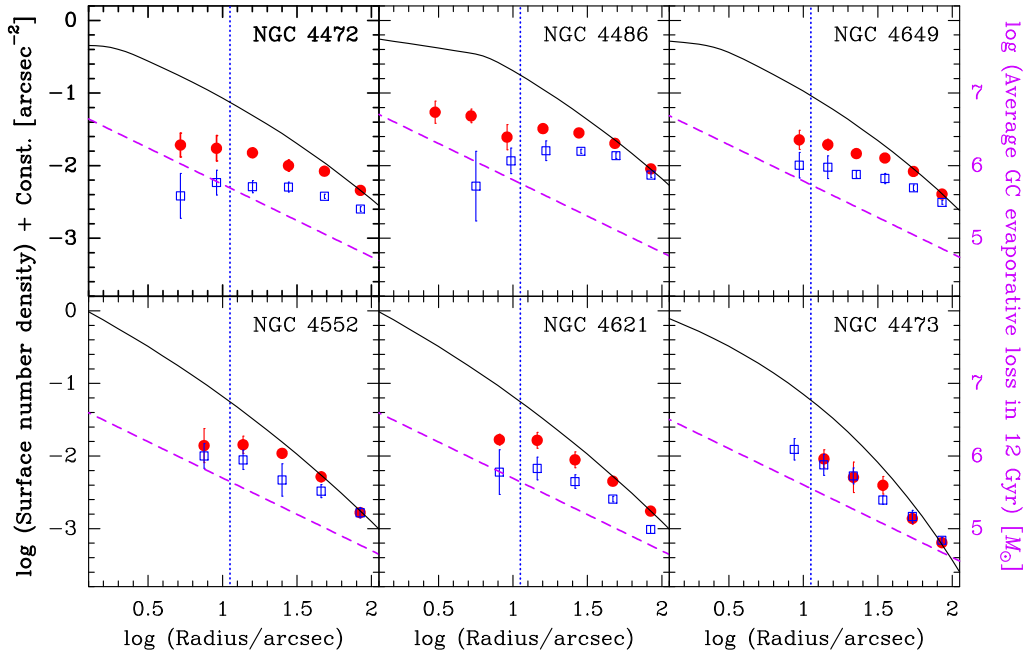


Figure 8. A copy of Figure 3 to which we added radial surface number density profiles of metal-poor GCs in each galaxy, shown with open blue squares. See discussion in Section 6.1.

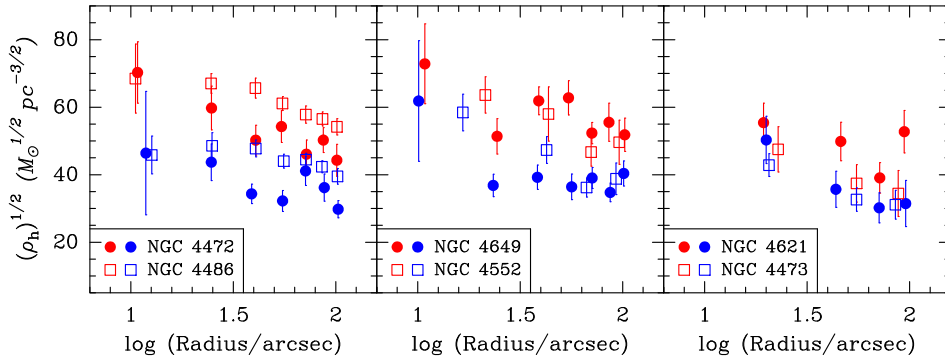


Figure 9. Radial profiles of the running average value of $\rho_h^{1/2}$ for the GC systems in the 6 ACSVCS galaxies shown in Figures 3 and 8. Blue symbols correspond to metal-poor GCs while red symbols correspond to metal-rich GCs. See legend for the associations between symbol types and galaxies. See discussion in Section 6.1.

the resulting $[\alpha/\text{Fe}]$, as observed. Similarly, the anticorrelation between $FUV-V$ and central velocity dispersion arises in this scenario due to the strong correlation between ETG luminosity (and thus likely mass as well) and the value of M_c of its GC system (see Section 5.1.3 and Johnson et al. 2017), in conjunction with the fact that $\mu_{\text{ev}} \propto \sigma$ (see Equation 2). This would also indirectly cause the anticorrelation between $FUV-V$ and $[Z/H]$, given the well-known mass-metallicity relation among ETGs (e.g., Ferrarese et al. 2006). The anticorrelation between $FUV-V$ and age would arise in part due to the age dependence of the production rate of EHB stars due to stellar evolution, and in part because the more massive ETGs (with higher values of M_c and μ_{ev}) typically have older SSP ages. Finally, the strong Burstein et al. (1988) anticorrelation between $FUV-V$ and Mg_2 can be explained by the sensitivities of the Mg_2 index to age, $[Z/H]$, and $[\alpha/\text{Fe}]$, all of which anticorrelate with $FUV-V$ (see also Jeong et al. 2012).

Zaritsky et al. (2015) recently reported a correlation between the strength of the UV upturn in ETGs and the stellar mass-to-light ratio inferred from SED fitting, suggesting that differences in the low-mass end of the stellar IMF are related

to the nature of the EHB stars responsible for the FUV flux in ETGs. In the context of the scenario on the nature of the UV upturn presented here, the relation found by Zaritsky et al. arises for the same reasons as that of the relation between M_c and ETG luminosity or mass, i.e., a scenario in which the central regions in massive ETGs contain relatively high mass fractions from massive galaxy building blocks, which formed their stars earlier and with higher SFR surface densities than less massive ones. Those very high SFR surface densities are also thought to cause the steep stellar IMFs at sub-solar masses found in the central regions of massive ETGs, specifically through strong turbulence (high Mach numbers), which causes cloud fragmentation to occur at relatively small scales (Hopkins 2013).

7. SUMMARY AND CONCLUSIONS

Prompted by the recent finding of FUV-bright massive GCs in M87, the central dominant galaxy in the Virgo cluster of galaxies (Sohn et al. 2006; Kaviraj et al. 2007), we investigate the idea that there is a physical connection between the UV upturn in ETGs and He-enhanced stellar populations in massive GCs. We study the dependencies of the strength of the

UV upturn in ETGs on the GC specific frequency S_N and other galaxy properties, mainly using results from the literature. We find that $FUV-V$ anticorrelates strongly with $S_{N, \text{red}}$, the specific frequency of red (metal-rich) GCs in ETGs. This anticorrelation appears to be causal, in that ETGs with high values of $S_{N, \text{red}}$ consistently lie “above” linear fits to the previously known anticorrelations between $FUV-V$ and Mg_2 , age, $[Z/H]$, and central velocity dispersion σ .

Guided by the observed depletion of surface number densities of metal-rich GCs in the inner regions of massive ETGs, which is where the UV upturn is known to occur, we explore the hypothesis that the UV upturn is produced mainly by He-enhanced populations formed within massive (mainly metal-rich) GCs that are subsequently disrupted by dynamical evolution in the strong tidal fields in the inner regions of ETGs during the $\gtrsim 10$ Gyr of their lifespan, using the observed FUV luminosities seen in the surviving massive GCs in M87 as proxies.

Adopting a Schechter (1976) function parameterization of GCMFs in conjunction with simulations of dynamical evolution of GCs, we find that the ranges of observed $FUV-V$ colors and FUV luminosities among ETGs are entirely consistent with our hypothesis if the initial masses of GCs responsible for the bulk of the FUV output were $M_0 \gtrsim 3 \times 10^5 M_\odot$. (This value for M_0 is formally an underestimate, since it does not account for the effects of rapid mass loss mechanisms during the first $\approx 10^8$ yr after GC formation.) This lower limit of the initial mass of GCs responsible for the UV upturn is consistent with the masses of the FUV-bright GCs currently seen in M87. Specifically, we find that the $FUV-V$ colors of the ETGs with the weakest UV upturns and lowest values of $S_{N, \text{red}}$ are consistent with GCs that were formed in environments featuring relatively low characteristic Schechter truncation masses ($M_c \approx 10^6 M_\odot$), likely associated with regions with relatively low SFR surface densities. Conversely, the $FUV-V$ colors of the ETGs with the strongest UV upturns and highest $S_{N, \text{red}}$ values are consistent with GC systems with $M_c \approx 10^7 M_\odot$, likely having formed in vigorously star-forming environments. Importantly, the values of M_c necessary to explain the range of $FUV-V$ seen among ETGs are consistent with the values of M_c found from evolved Schechter function fits of the GC luminosity functions of those ETGs. Furthermore, we find

that this range of M_c found among ETGs also explains the correlation between $FUV-V$ and $S_{N, \text{red}}$ in that GCMFs with larger values of M_c have wider GCMFs, which translates to larger values of S_N due to the way S_N is defined.

If the scenario proposed here is correct, an important implication would be that the He-enhanced populations responsible for the UV upturn in ETGs should show light-element abundance ratios similar to those observed within massive GCs, i.e., enhancements of $[\text{Na}/\text{Fe}]$ and $[\text{N}/\text{Fe}]$ accompanied by depletions of $[\text{C}/\text{Fe}]$ and $[\text{O}/\text{Fe}]$. Encouragingly, a recent spectroscopic study of massive ETGs by van Dokkum et al. (2017) does show evidence for radial gradients of $[\text{Na}/\text{Fe}]$ and $[\text{O}/\text{Fe}]$ in the sense predicted by this scenario. As such, we predict that future studies will also find radial gradients in $[\text{N}/\text{Fe}]$ that increase toward galaxy centers in massive ETGs, and that such radial gradients have the largest amplitudes in ETGs that have the strongest UV upturns.

Our findings suggest that the nature of the UV upturn in ETGs and the variation of its strength among ETGs are causally related to that of helium-rich populations in massive GCs, rather than intrinsic properties of field stars in massive galactic spheroids. The observed ranges of both $FUV-V$ and $S_{N, \text{red}}$ among ETGs can be explained by the observed range in M_c of their GC systems, which in turn can be explained by a range of SFR surface density occurring in the progenitors of the present-day ETGs, with the more massive ETGs containing higher mass fractions from more massive protogalaxies, which formed their stars earlier and with higher SFR surface densities than the less massive ones.

I thank the anonymous referee for a very thoughtful report with relevant and helpful suggestions. I also acknowledge useful discussions with Thomas Puzia, Tom Brown, Marcio Catelán, and Diederik Kruijssen. This research made use of the HyperLeda database (<http://leda.univ-lyon1.fr>). This research has made use of the NASA/IPAC Extragalactic Database (NED), which is operated by the Jet Propulsion Laboratory, California Institute of Technology, under contract with the National Aeronautics and Space Administration. This paper is based in part on observations made with the NASA Galaxy Evolution Explorer (GALEX). GALEX was operated for NASA by the California Institute of Technology under NASA contract NAS5-98034.

APPENDIX

A COMPARISON OF METALLICITIES OF METAL-RICH GCs IN M87 WITH THE UNDERLYING FIELD POPULATION

For the specific case of GCs in M87, the available spectroscopic data in the literature (Cohen et al. 1998) are, unfortunately, strongly dominated by GCs at large galactocentric distances, and thus by metal-poor GCs. Furthermore, the S/N ratio of a significant fraction of the GC spectra of Cohen et al. (1998) are not high enough to derive ages and metallicities at the $\sim 50\%$ accuracy level ($S/N \sim 30$ per Å, see Puzia et al. 2005), thus providing only marginal constraints on the age and metallicity of these GCs. To reduce the resulting uncertainty on the assignment of GCs targeted by Cohen et al. (1998) as “metal-poor” versus “metal-rich,” we use the $U-R_J$ (where R_J is Johnson R) colors from Strom et al. (1981), whose GC target list was used by Cohen et al. (1998). The selection of metal-poor (or metal-rich) GCs was made by selecting GCs bluer (or redder) than the $U-R_J$ color associated with the metallicity corresponding to the dip in $g-z$ between the blue and red peaks in the bimodal color distribution in the high-quality ACSVCS photometry of M87 ($g-z = 1.20$, Peng et al. 2006). In this context, we use BC03 model SEDs for an age of 12 Gyr and a Chabrier (2003) IMF, and derive model $U-R_J$ colors by using the SYNPHOT package within IRAF/STSDAS. The resulting $U-R_J$ color to discriminate metal-poor from metal-rich GCs in M87 is 1.75. To evaluate mean metallicities for the metal-poor and metal-rich GCs, we use the indices $H\beta$ and $[\text{MgFe}]'$, respectively, and compare them to predictions of the SSP models of Thomas et al. (2003). Figure 10 shows $H\beta$ versus $[\text{MgFe}]'$ for the GCs in M87 from Cohen et al. (1998). The metal-poor and metal-rich GCs selected as such by means of their $U-R_J$ colors from Strom et al. (1981) are shown with blue and red circles, respectively. Since the uncertainties are significant for the individual GCs, we also indicate inverse-variance-weighted average indices for the metal-poor and metal-rich GCs selected as mentioned above (see large blue and

red squares in Figure 10). Note that $[Z/H] \approx -0.25$ for the weighted average metal-rich GC, for which $2'' \leq R_{\text{gal}} \leq 390''$ with a median of $181''$. For comparison, we overplot $H\beta$ and $[MgFe]'$ for the diffuse light of M87 at $R_{\text{gal}} \sim 40''$, the outermost data point from Davies et al. (1993) and Sarzi et al. (2018). Note that the age and metallicity of the latter are consistent with those of the average metal-rich GC in M87 to within 1σ . We conclude that the available spectroscopic observations of M87 and its GCs are consistent with previous evidence for other ETGs (see Goudfrooij & Kruijssen 2013 and references therein) in that the mean metallicities of metal-rich GCs and the underlying field stars in giant ETGs are consistent with each other.

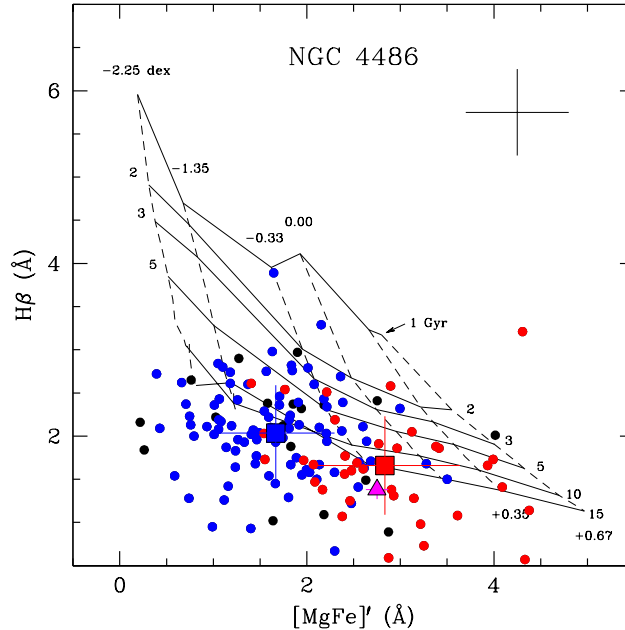


Figure 10. $H\beta$ versus $[MgFe]'$ for GCs in NGC 4486 (= M87) from the data of Cohen et al. (1998). Small blue and red circles indicate GCs designated metal-poor and metal-rich, respectively, by means of $U-R_J$ colors from Strom et al. (1981). Large filled blue and red squares represent weighted average values of $H\beta$ and $[MgFe]'$ of the metal-poor and metal-rich GCs, respectively. GCs. SSP models of Thomas et al. (2003) are overplotted for $[\alpha/Fe] = +0.3$. Dashed lines indicate $[Z/H]$ values of -2.25 , -1.35 , -0.33 , 0.00 , 0.35 , and 0.67 dex. Solid lines indicate ages of 1, 2, 3, 5, 10, and 15 Gyr. For comparison, the magenta triangle represents $H\beta$ and $[MgFe]'$ for the diffuse light of NGC 4486 at $R_{\text{gal}} = 40''$. See discussion in Appendix A.

REFERENCES

- Adams, F. C., & Myers, P. 2001, *ApJ*, 533, 744
Ashman, K. M., & Zepf, S. E., 1992, *ApJ*, 384, 50
Ashman, K. M., Bird, C. M., & Zepf, S. E. 1994, *AJ*, 108, 2348
Bassino, L. P., Richtler, T., & Dirsch, B., 2006, *MNRAS*, 367, 156
Bastian, N., Konstantopoulos, I. S., Trancho, G., et al. 2012, *A&A*, 541, A25
Baumgardt, H., Kroupa, P., & Parmentier, G. 2008, *MNRAS*, 384, 1231
Bekki, K. 2012, *ApJ*, 747, 78
Bertola, F. 1980, *Highlights of Astronomy*, 5, 311
Binney, J., & Tremaine, S. 1987, *Galactic Dynamics*, Princeton Series in Astrophysics (Princeton, NJ: Princeton University Press)
Boselli, A., Cortese, L., Deharveng, J. M., et al. 2005, *ApJL*, 629, L29
Brodie, J. P., & Strader, J. 2006, *ARA&A*, 44, 193
Brodie, J. P., Usher, C., Conroy, C., et al. 2012, *ApJL*, 759, L33
Brown, T. M., Ferguson, H. C., Davidsen, A. F., & Dorman, B. 1997, *ApJ*, 482, 685
Brown, T. M., Sweigart, A. V., Lanz, T., et al. 2010, *ApJ*, 718, 1332
Brown, T. M., Cassisi, S., D'Antona, F., et al. 2016, *ApJ*, 822, 44
Bruzual, G. A., & Charlot, S., 2003, *MNRAS*, 344, 1000
Bureau, M., Jeong, H., Yi, S. K., et al. 2011, *MNRAS*, 414, 1887
Burgarella, D., Kissler-Patig, M., & Buat, V. 2001, *AJ*, 121, 2647
Burstein, D., Davies, R. L., Dressler, A., et al. 1987, *ApJS*, 64, 601
Burstein, D., Bertola, F., Buson, L. M., Faber, S. M., & Lauer, T. R. 1988, *ApJ*, 328, 440
Caloi, V., & D'Antona, F. 2007, *A&A*, 463, 949
Caon, N., Capaccioli, M., & D'Onofrio, M. 1993, *MNRAS*, 265, 1013
Cardelli, J. A., Clayton, G. C., & Mathis, J. S. 1989, *ApJ*, 345, 245
Carretta, E., Bragaglia, A., Gratton, R. G., et al. 2010, *A&A*, 505, 117
Carter, D., Pass, S., Kennedy, J., Karick, A. M., & Smith, R. J. 2011, *MNRAS*, 414, 3410
Cassisi, S., Salaris, M., Pietrinferi, A., & Hyder, D. 2017, *MNRAS*, 464, 2341
Chabrier, G. 2003, *PASP*, 115, 763
Chandar, R., Whitmore, B. C., & Fall, S. M. 2010, *ApJ*, 713, 1343
Chung, C., Yoon, S.-J., & Lee, Y.-W. 2011, *ApJ*, 740, L45
Chung, C., Yoon, S.-J., & Lee, Y.-W. 2017, *ApJ*, 842, 91
Code, A. D., & Welch, G. A. 1979, *ApJ*, 229, 95
Cohen, J. G., Blakeslee, J. P., & Rhyzov, A. 1998, *ApJ*, 496, 808
Conroy, C. 2012, *ApJ*, 758, 21
Conroy, C., & van Dokkum, P. G. 2012, *ApJ*, 760, 71
Côté, P., Blakeslee, J. P., Ferrarese, L., et al. 2004, *ApJS*, 153, 223
Davies, R. L., Sadler, E. M., & Peletier, R. F. 1993, *MNRAS*, 262, 650
D'Ercole, A., Vesperini, E., D'Antona, F., McMillan, S. L. W., & Recchi, S. 2008, *MNRAS*, 391, 825
de Zeeuw, P. T., Bureau, M., Emsellem, E., et al. 2002, *MNRAS*, 329, 513
Dinescu, D. I., Girard, T. M., & van Altena, W. F. 1999, *AJ*, 117, 1792
Dirsch, B., Schuberth, Y., & Richtler, T., 2005, *A&A*, 433, 43
Dorman, B., O'Connell, R. W., & Rood, R. T. 1995, *ApJ*, 442, 105
Dotter, A., Chaboyer, B., Jevremoić, D., et al. 2007, *AJ*, 134, 376
Eisenhardt, P. R., De Propris, R., Gonzalez, A. H., et al. 2007, *ApJS*, 169, 225
Elmegreen, B. G., & Efremov, Yu. N. 1997, *ApJ*, 480, 235
Fall, S. M., & Zhang, Q. 2001, *ApJ*, 561, 751
Ferrarese, L., Côté, P., Jordán, A., et al. 2006, *ApJS*, 164, 334
Forbes, D. A. 2005, *ApJL*, 635, L137
Forbes, D. A., Grillmair, C. J., Williger, G. M., Elson, R. A. W., & Brodie, J. P. 1998, *MNRAS*, 293, 325
Forbes, D. A., Sánchez-Blázquez, P., Phan, A. T. T., et al. 2006, *MNRAS*, 366, 1230
Geisler, D., Lee, M. G., & Kim, E. 1996, *AJ*, 111, 1529
Genzel, R., Tacconi, L. J., Gracia-Carpio, J., et al. 2010, *MNRAS*, 407, 2091
Georgiev, I. Y., Puzia, T. H., Goudfrooij, P., & Hilker, M. 2010, *MNRAS*, 406, 1967
Gnedin, O. Y., & Ostriker, J. P. 1997, *ApJ*, 474, 223
Goudfrooij, P., Hansen, L., Jørgensen, H. E., et al. 1994a, *A&AS*, 104, 179
Goudfrooij, P., Nørgaard-Nielsen, H. U., Hansen, L., & Jørgensen, H. E. 1994b, *A&AS*, 105, 341

- Goudfrooij, P., & Trinchieri, G. 1998, *A&A*, 330, 123
- Goudfrooij, P., Alonso, M. V., Maraston, C., & Minniti, D. 2001, *MNRAS*, 328, 237
- Goudfrooij, P., Schweizer, F., Gilmore, D., & Whitmore, B. C. 2007, *AJ*, 133, 2737
- Goudfrooij, P., Puzia, T. H., Chandar, R., & Kozhurina-Platais, V. 2011, *ApJ*, 737, 4
- Goudfrooij, P., & Kruijssen, J. M. D. 2013, *ApJ*, 762, 107
- Goudfrooij, P., & Kruijssen, J. M. D. 2014, *ApJ*, 780, 43
- Goudfrooij, P., & Fall, S. M. 2016, *ApJ*, 833, 8
- Gratton, R., Carretta, E., & Bragaglia, A. 2012, *A&A Rev.*, 20, 50
- Greggio, L., & Renzini, A. 1990, *ApJ*, 364, 35
- Han, Z., Podsiadlowski, Ph., & Lynas-Gray, A. E. 2007, *MNRAS*, 380, 1098
- Hansen, L., Nørgaard-Nielsen, H. U., & Jørgensen, H. E. 1985, *A&A*, 149, 442
- Harris, W. E., & van den Bergh, S. 1981, *AJ*, 86, 1627
- Harris, W. E., Harris, G. L. H., Layden, A. C., & Wehner, E. M. H. 2007, *ApJ*, 666, 903
- Harris, W. E., Spitzer, L. R., Forbes, D. A., & Bailin, J. 2010, *MNRAS*, 401, 1965
- Harris, W. E., Harris, G. L. H., & Alessi, M. 2013, *ApJ*, 772, 82
- Harris, W. E., Ciccone, S. M., Eadie, G. M., et al. 2017, *ApJ*, 835, 101
- Hills, J. G. 1980, *ApJ*, 235, 986
- Hopkins, P. F. 2013, *MNRAS*, 433, 170
- Jennings, Z. G., Strader, J., Romanowsky, A. J., et al. 2014, *AJ*, 148, 32
- Jeong, H., Yi, S. K., Bureau, M., et al. 2012, *MNRAS*, 423, 1921
- Johnson, L. C., Seth, A. C., Dalcanton, J. J., et al. 2017, *ApJ*, 839, 78
- Jordán, A., McLaughlin, D. E., Côté, P., et al. 2007, *ApJS*, 171, 101
- Jordán, A., Peng, E. W., Blakeslee, J. P., et al. 2009, *ApJS*, 180, 54
- Jordán, A., Peng, E. W., Blakeslee, J. P., et al. 2015, *ApJS*, 221, 13
- Kaviraj, S., Sohn, S. T., O'Connell, R. W., et al. 2007, *MNRAS*, 377, 987
- King, I. 1962, *AJ*, 67, 471
- Kroupa, P. 2001, *MNRAS*, 322, 231
- Kruijssen, J. M. D. 2015, *MNRAS*, 454, 1658
- Kundu, A., Whitmore, B. C., Sparks, W. B., et al. 1999, *ApJ*, 513, 733
- Kuntschner, H. 2000, *MNRAS*, 315, 184
- Kuntschner, H., Emsellem, E., Bacon, R., et al. 2010, *MNRAS*, 408, 97
- La Barbera, F., Ferreras, I., Vazdekis, A., et al. 2013, *MNRAS*, 433, 3017
- Lada, C. J., & Lada, E. A. 2003, *ARA&A*, 41, 57
- Lauer, T. R., Faber, S. M., Gebhardt, K., et al. 2005, *AJ*, 129, 2138
- Law, D. R., Steidel, C. C., Erb, D. K., et al. 2009, *ApJ*, 697, 2057
- Law, D. R., Steidel, C. C., Shapley, A. E., et al. 2012, *ApJ*, 759, 29
- Lee, H. M., & Goodman, J. 1995, *ApJ*, 443, 109
- Li, H., Gnedin, O. Y., Gnedin, N. Y., et al. 2017, *ApJ*, 834, 69
- Martel, A. R., Ford, H. C., Bradley, L. D., et al. 2004, *AJ*, 128, 2758
- Martin, D. C., Fanson, J., Schiminovich, D., et al. 2005, *ApJL*, 619, L1
- Masegosa, J., Márquez, I., Ramirez, A., & González-Martín, O. 2011, *A&A*, 527, A23
- McDermid, R. M., Cappelari, M., Alatalo, K., et al. 2014, *ApJL*, 792, L37
- McLachlan, G. J., & Basford, K. E. 1988, *Mixture Models: Inference and Application to Clustering* (New York: M. Dekker)
- McLaughlin, D. E., & Fall, S. M. 2008, *ApJ*, 679, 1272
- Miller, B. W., & Lotz, J. M. 2007, *ApJ*, 670, 1074
- Milone, A. P. 2015, *MNRAS*, 446, 1672
- Milone, A. P., Piotto, G., Renzini, A., et al. 2017, *MNRAS*, 464, 3636
- Moore, B., Diemand, J., Madau, P., Zemp, M., & Stadel, J. 2006, *MNRAS*, 368, 563
- Morrissey, P., Schiminovich, D., Barlow, T. A., et al. 2005, *ApJL*, 619, L7
- O'Connell, R. W. 1999, *ARA&A*, 37, 603
- O'Connell, R. W., Bohlín, R. C., Collins, N. R., et al. 1992, *ApJL*, 395, L45
- Ohl, R. G., O'Connell, R. W., Bohlín, R. C., et al. 1998, *ApJL*, 505, L11
- Park, J.-H., & Lee, Y.-W. 1997, *ApJ*, 476, 28
- Peacock, M. B., Strader, J., Romanowsky, A. J., & Brodie, J. P. 2015, *ApJ*, 800, 13
- Peacock, M. B., Zepf, S. E., Kundu, A., & Chael, J. 2017, *MNRAS*, 464, 713
- Peletier, R. F., Davies, R. L., Illingworth, G. D., Davis, L. E., & Cawson, M. 1990, *AJ*, 100, 1091
- Peng, E. W., Jordán, A., Côté, P., et al. 2006, *ApJ*, 639, 95
- Peng, E. W., Jordán, A., Côté, P., et al. 2008, *ApJ*, 681, 197
- Persson, S. E., Frogel, J. A., & Aaronson, M. 1979, *ApJS*, 39, 61
- Piotto, G., Bedin, L. R., Anderson, J., et al. 2007, *ApJL*, 661, L53
- Portegies Zwart, S. F., McMillan, S. L. W., & Gieles, M. 2010, *ARA&A*, 48, 431
- Puzia, T. H., Kissler-Patig, M., Thomas, D., et al. 2005, *A&A*, 439, 997
- Puzia, T. H., Kissler-Patig, M., & Goudfrooij, P. 2006, *ApJ*, 648, 383
- Puzia, T. H., Paolillo, M., Goudfrooij, P., et al. 2014, *ApJ*, 786, 78
- Rejkuba, M., Harris, W. E., Greggio, L., et al. 2014, *ApJL*, 791, L2
- Renzini, A., D'Antona, F., Cassisi, S., et al. 2015, *MNRAS*, 454, 4197
- Rhode, K. L., & Zepf, S. E. 2001, *AJ*, 127, 302
- Rich, R. M., Sosin, C., Djorgovski, S., et al. 1997, *ApJL*, 484, L25
- Rich, R. M., Salim, S., Brinchmann, J., et al. 2005, *ApJL*, 619, L107
- Roediger, J. C., Courteau, S., Graves, G., & Schiavon, R. P. 2014, *ApJS*, 210, 10
- Salpeter, E. E. 1955, *ApJ*, 121, 161
- Sánchez-Blázquez, P., Gorgas, J., Cardiel, N., & González, J. J. 2006, *A&A*, 457, 787
- Sarzi, M., Spiniello, C., La Barbera, F., Krajnović, D., & van den Bosch, R. 2018, submitted to *MNRAS* ([arXiv:1711.0898](https://arxiv.org/abs/1711.0898))
- Schechter, P. 1976, *ApJ*, 203, 297
- Schiavon, R. P. 2007, *ApJS*, 171, 146
- Schiavon, R. P., Caldwell, N., Conroy, C., et al. 2013, *ApJL*, 776, L7
- Schlegel, D. J., Finkbeiner, D. P., & Davis, M. 1998, *ApJ*, 500, 525
- Sikkema, G., Peletier, R. F., Carter, D., Valentijn, E. A., & Balcells, M. 2006, *A&A*, 458, 458
- Smith, R. J., Lucey, J. R., & Carter, D. 2012a, *MNRAS*, 421, 2982
- Smith, R. J., Lucey, J. R., & Carter, D. 2012b, *MNRAS*, 426, 2994
- Snedden, C., Kraft, R. P., Prosser, C. F., & Langer, G. E. 1992, *AJ*, 104, 2121
- Sohn, S. T., O'Connell, R. W., Kundu, A., et al. 2006, *AJ*, 131, 866
- Spiniello, C., Trager, S., Koopmans, L. V. E., & Conroy, C. 2014, *MNRAS*, 438, 1483
- Spitzer, L. Jr. 1987, *Dynamical Evolution of Globular Clusters* (Princeton: Princeton University Press)
- Spolaor, M., Forbes, D. A., Hau, G. K. T., Proctor, R. N., & Brough, S. 2008, *MNRAS*, 385, 667
- Strader, J., Romanowsky, A. J., Brodie, J. P., et al. 2011, *ApJS*, 197, 33
- Strom, S. E., Forte, J. C., Harris, W. E., et al. 1981, *ApJ*, 245, 416
- Tacconi, L. J., Neri, R., Genzel, R., et al. 2013, *ApJ*, 768, 74
- Tailo, M., D'Antona, F., Milone, A. P., et al. 2017, *MNRAS*, 465, 1046
- Tantalo, R., Chiosi, C., Bressan, A., & Fagotto, F. 1996, *A&A*, 311, 361
- Thomas, D., Maraston, C., & Bender, R. 2003, *MNRAS*, 339, 897
- Thomas, D., Maraston, C., Bender, R., & Mendes de Oliveira, C. 2005, *ApJ*, 621, 673
- Trager, S. C., Worthey, G., Faber, S. M., Burstein, D., & González, J. J. 1998, *ApJS*, 116, 1
- van Dokkum, P. G., & Conroy, C. 2010, *Nature*, 468, 940
- van Dokkum, P. G., & Franx, M. 1995, *AJ*, 110, 2027
- van Dokkum, P. G., Conroy, C., Villaume, A., Brodie, J. P., & Romanowsky, A. J. 2017, *ApJ*, 841, 68
- Vazdekis, A., Sánchez-Blázquez, P., Falcón-Barroso, J., et al. 2010, *MNRAS*, 404, 1639
- Ventura, P., Di Criscienzo, M., Carini, R., & D'Antona, F. 2013, *MNRAS*, 431, 3642
- Vesperini, E., McMillan, S. L. W., & Portegies Zwart, S. 2009, *ApJ*, 698, 615
- Whitmore, B. C., Chandar, R., Bowers, A. S., et al. 2014, *AJ*, 147, 78
- Yi, S. 2008, in "Hot Subdwarf Stars and Related Objects", eds. U. Heber, S. Jeffery, & R. Napiwotzki (ASP: San Francisco), p. 3
- Yi, S., Demarque, P., & Oemler, A. 1997, *ApJ*, 486, 201
- Zaritsky, D., Gil de Paz, A., & Bouquin, A. Y. K. 2015, *MNRAS*, 446, 2030
- Zhang, Q., & Fall, S. M. 1999, *ApJ*, 527, L81